



Tibetan and Indian lithospheres in the upper mantle beneath Tibet: Evidence from broadband surface-wave dispersion

Matthew R. Agius

Geophysics Section, School of Cosmic Physics, Dublin Institute for Advanced Studies, 5 Merrion Square, Dublin, Ireland (matthew@cp.dias.ie)

Physics Department, Faculty of Science, University of Malta, Msida, Malta

Sergei Lebedev

Geophysics Section, School of Cosmic Physics, Dublin Institute for Advanced Studies, Dublin, Ireland

[1] Broadband seismic experiments over the last two decades have produced dense data coverage across Tibet. Yet, the mechanism of the India-Asia lithospheric convergence beneath it remains a puzzle, with even its basic features debated and with very different end-member models advocated today. We measured highly accurate Rayleigh- and Love-wave phase-velocity curves in broad period ranges (up to 5–200 s) for a few tens of pairs and groups of stations across Tibet, combining, in each case, hundreds to thousands of interstation measurements made with cross-correlation and waveform-inversion methods. Robust shear-velocity profiles were then determined by extensive series of nonlinear inversions of the data, designed to constrain the depth-dependent ranges of isotropic-average shear speeds and radial anisotropy. Temperature anomalies in the upper mantle were estimated from shear velocities using accurate petrophysical relationships. Our results reveal strong heterogeneity in the upper mantle beneath Tibet. Very large high-velocity anomalies in the upper mantle are consistent with the presence of underthrust (beneath southwestern Tibet) and subducted (beneath central and eastern Tibet) Indian lithosphere. The corresponding thermal anomalies match those estimated for subducted Indian lithosphere. In contrast to the Indian lithosphere, Tibetan lithosphere and asthenosphere display low-to-normal shear speeds; Tibetan lithosphere is thus warm and thin. Radial anisotropy in the upper mantle is weak in central and strong in northeastern Tibet, possibly reflecting asthenospheric flow above the subducting Indian lithospheric slab.

Components: 14,576 words, 12 figures, 1 table.

Keywords: Tibetan; Indian; lithosphere; subduction; shear speed; upper mantle.

Index Terms: 7218 Lithosphere: Seismology; 7240 Subduction zones: Seismology; 7255 Surface waves and free oscillations: Seismology; 1236 Rheology of the lithosphere and mantle: Geodesy and Gravity.

Received 25 June 2013; **Revised** 11 September 2013; **Accepted** 18 September 2013; **Published** 17 October 2013.

Agius, M. R. and S. Lebedev (2013), Tibetan and Indian lithospheres in the upper mantle beneath Tibet: Evidence from broadband surface-wave dispersion, *Geochem. Geophys. Geosyst.*, 14, 4260–4281, doi:10.1002/ggge.20274.



1. Introduction

[2] The uplift and evolution of the Tibetan Plateau (Figure 1) have long been recognized to be driven by India's convergence with Asia [Argand, 1924; Molnar and Tapponnier, 1975]. The tectonic blocks that make up the plateau [Allègre *et al.*, 1984] experienced deformation associated with the convergence already during the Cretaceous northward subduction of the Indo-Australian oceanic lithosphere beneath them [England and Searle, 1986]. The Tethyan oceanic slabs have by now sunken into deep mantle [Van der Voo *et al.*, 1999; Hafkenscheid *et al.*, 2006; Replumaz *et al.*, 2010a; Zahirovic *et al.*, 2012]. Following the closure of the Tethys Ocean, the thrusting of Indian continental lithosphere beneath the Himalayas and the Lhasa Terrane has been thought to have taken place for the last ~50 Myr [e.g., Allègre *et al.*, 1984; Yin and Harrison, 2000], although it has recently been proposed that the collision of thick, contiguous Indian continental lithosphere with Asia occurred only later, around 40 Ma [Zahirovic *et al.*, 2012], 34 Ma [Aitchison *et al.*, 2007], or even 25–20 Ma [van Hinsbergen *et al.*, 2012]. It is estimated that India and Asia converged by up to 3600 km since 52 Myr, with over 1000 km of north–south shortening absorbed by the Himalaya and Tibet [Yin and Harrison, 2000; Guillot *et al.*, 2003; van Hinsbergen *et al.*, 2011].

[3] The convergence of the strong cratonic lithosphere of India and the weaker lithosphere of Tibet has built the Himalaya mountain range and raised, behind it, the Tibetan Plateau, with its flat relief relative to its high elevation [Hatzfeld and Molnar, 2010]. The mechanism of this convergence remains unclear. The properties and configuration of the Tibetan and Indian lithospheres in the upper mantle beneath Tibet are debated, with contrasting competing models proposed.

[4] The three main end-member models of the lithospheric convergence include underthrusting, subduction, and viscous thickening of the lithosphere. Different scenarios falling under one of the three types of models are shown in Figure 2; we note that each of the three end-member models may apply beneath different parts of the plateau.

[5] Underthrusting of India far north beneath the Tibetan Plateau has been proposed by Argand [1924]. In this paper we refer to underthrusting as the scenario in which the Indian lithosphere slides directly beneath the Tibetan lithosphere, with no asthenospheric window between them [e.g., Ni

and Barazangi, 1984; Powell, 1986; Owens and Zandt, 1997]. The underthrusting of India beneath the entire length of the Himalayas, for example, is beyond doubt [e.g., Ni and Barazangi, 1984; Nábelek *et al.*, 2009; Liang *et al.*, 2011]. Further north, it may occur only in certain parts of the plateau. Beneath western Tibet, high seismic velocities have been detected in the shallow mantle using both body waves [Barazangi and Ni, 1982; McNamara *et al.*, 1997; Huang and Zhao, 2006; Li *et al.*, 2008] and surface waves [Shapiro and Ritzwoller, 2002; Friederich, 2003; Priestley *et al.*, 2006; Lebedev and van der Hilst, 2008], suggesting underthrusting of the Indian lithosphere beneath western Tibet as far northward as the Tarim Basin [Barazangi and Ni, 1982; Li *et al.*, 2008]. Consistent with this scenario, “flat-lying” *S*-to-*P* phase conversions from *S* receiver functions in western Tibet have been interpreted as the Indian and Asian lithosphere–asthenosphere boundaries (LAB), meeting near the northern boundary of the plateau [Zhao *et al.*, 2010; Kind and Yuan, 2010].

[6] The second end-member model is lithospheric subduction, which we define as the sliding of the lithosphere into the asthenosphere (the Tibetan lithosphere above and the Indian lithosphere below being separated by a layer of asthenosphere). The different modes of subduction beneath Tibet include shallow-angle, steep-angle, northward and southward subduction (Figure 2). Steep-angle, northward subduction of India has been proposed in parts of southern Tibet based on *P*-wave, travel-time tomography [Tilmann *et al.*, 2003; Huang and Zhao, 2006; Li *et al.*, 2008]. The tomographic models showed high-velocity anomalies extending from north Indian uppermost mantle down to 300 km depth beneath southern Tibet, north of the Yarlung-Zangbo Suture. This was seen, however, only in one particular segment within Tibet (87°E–90°E), and recent tomography using larger, new data sets prompted an inference that the previously imaged subvertical, high-velocity structure may in fact comprise two separate anomalies, with recently subducted Indian lithosphere located above a lithospheric fragment subducted earlier [Liang *et al.*, 2012; Yue *et al.*, 2012; C. Nunn *et al.*, *P*- and *S*-body wave tomographic model of the northeastern Tibetan Plateau and its margins with additional constraints from surface wave tomography, submitted to *Geophysical Journal International*, 2012]. In northern and northeastern Tibet, north of the Bangong-Nujiang Suture (BNS), most travel-time tomographic models

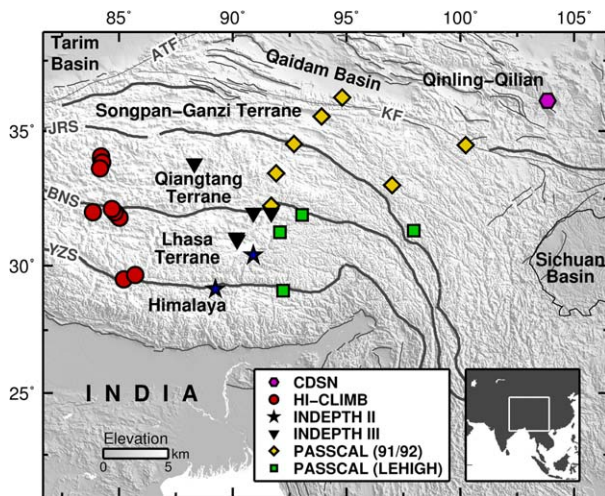


Figure 1. A map of Tibet and surroundings. Seismic stations used in this study are shown with different symbols indicating different networks. Black lines indicate sutures and faults: YZS (Yarlung-Zangbo Suture), BNS (Bangong-Nujiang Suture), JRS (Jinsha River Suture), KF (Kunlun Fault), and ATF (Altyn Tagh Fault); the sutures divide Tibet into major terranes. Inset shows the location of the map region within Asia.

show low wave speeds in the entire upper mantle. Exceptions include recent regional models of Zhang *et al.* [2012] (high velocities in eastern Tibet's upper mantle up to and a little north of the BNS) and Liang *et al.* [2012] (smaller-scale high-velocity anomalies beneath eastern Lhasa and

Qiangtang Terranes), as well as the earlier study of Zhou and Murphy [2005], who mapped *P*-velocity anomalies below Tibet using a global model and inferred subhorizontal subduction of the Indian lithospheric slab to depths of 165–260 km beneath nearly the entire Tibetan plateau, with an asthenospheric layer above it at 120–165 km depths. Chemenda *et al.* [2000] also argued for shallow-angle subduction of the Indian lithosphere, as part of a complex evolutionary model that included multiple slab break-offs and was based on thermomechanical laboratory modeling. Regional surface-wave tomography using new array data in central and eastern Tibet [Ceylan *et al.*, 2012] showed high wave speeds at around 150 km depth from the Himalaya to the Lhasa and Qiangtang Terranes (as far north as 34°N–35°N), with low velocities further north (36°N–37°N).

[7] Southward subduction of Asia beneath north-eastern Tibet has also been proposed [e.g., Willett and Beaumont, 1994; Tapponnier *et al.*, 2001]. Evidence for it has been inferred from some of the *P* and *S* receiver-function studies performed to date [Kosarev *et al.*, 1999; Kind *et al.*, 2002; Kumar *et al.*, 2006; Zhao *et al.*, 2011], although other studies have reported no evidence for such southward subduction [Zhao *et al.*, 2010; Liang *et al.*, 2012; Yue *et al.*, 2012].

[8] The third end-member model of lithospheric convergence beneath Tibet is viscous lithospheric

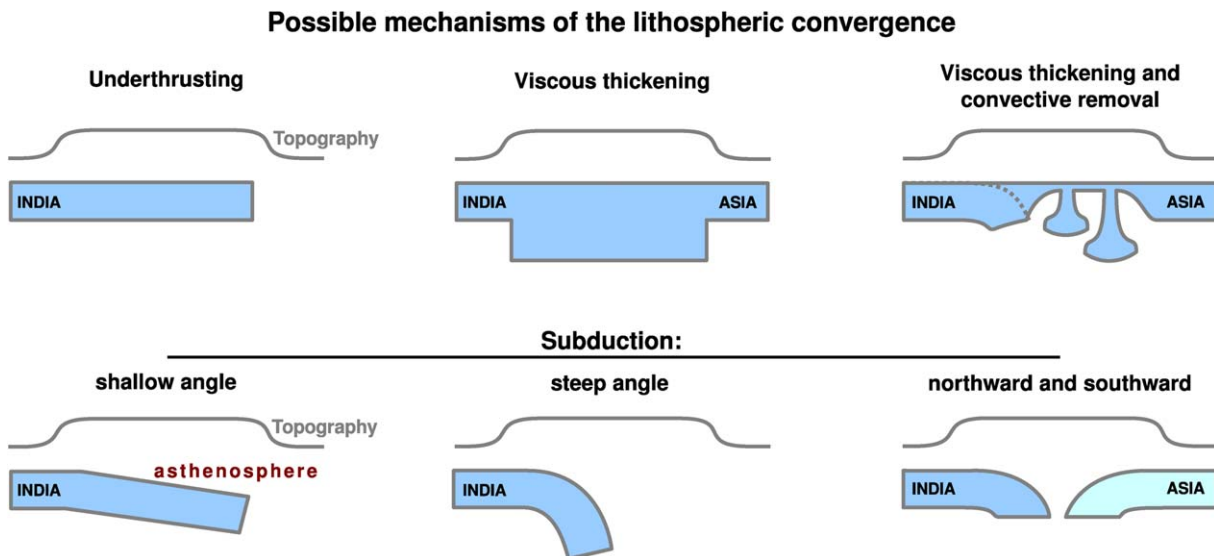


Figure 2. Conceptual models for the India-Asia lithospheric convergence beneath Tibet. The three main, end-member models include underthrusting of India's lithosphere beneath Tibet, viscous thickening of the lithosphere, and subduction.



thickening [e.g., England and Houseman, 1986; Dewey et al., 1988; Clark, 2012]. In one of the proposed scenarios, the mantle lithosphere thickens and remains intact, while in another scenario the thickened lithosphere becomes destabilized, with parts of it removed convectively and sinking into deep mantle (Figure 2). McKenzie and Priestley [2008] compared the high-velocity anomalies resolved by surface-wave tomography beneath Tibet and beneath cratons and suggested that a craton was forming beneath Tibet today. They proposed that the shortening of the lithospheric mantle could thicken the lithosphere and transport depleted material downward, to form a cratonic root. They argued, further, that the crust was insulated from the convecting mantle and that crustal radioactive heating was responsible for the lower V_S in the uppermost mantle, just beneath the Mohorovičić discontinuity (Moho). The alternative scenario [e.g., Houseman et al., 1981; Molnar et al., 1993; Hatzfeld and Molnar, 2010; Jiménez-Munt et al., 2008] invokes convective removal of Tibet's thickened mantle lithosphere, with the lower lithosphere dripping into cold, sinking plumes and the warm asthenosphere flowing in to replace it.

[9] In spite of decades of intensive study, there is surprisingly little agreement, as of today, regarding even the most basic features of the lithospheric configuration beneath Tibet. What is the fate of the Indian lithosphere that has descended beneath the Himalaya? Is it still within the upper mantle beneath Tibet? What is the thermal structure, thickness, and mechanical properties of the lithosphere of Tibet itself? What are the basic mechanisms of the lithospheric convergence?

[10] Recent surface-wave tomographic models, both global [Shapiro and Ritzwoller, 2002; Lebedev and van der Hilst, 2008; Schaeffer and Lebedev, 2013] (Figure 3) and regional [Friederich, 2003; Priestley et al., 2006; Kustowski et al., 2008; Panning et al., 2012], show low shear-wave speeds in the uppermost mantle beneath northern and eastern Tibet, confirming the earlier, 1-D shear-velocity models inferred from surface waves [e.g., Brandon and Romanowicz, 1986; Curtis and Woodhouse, 1997; Rapine et al., 2003]. At greater depths (~200 km), surface-wave tomography shows high S velocities (V_S). Intriguingly, most of the recent body-wave models, in contrast to surface-wave ones, do not display high-velocity anomalies in the upper mantle beneath central and northern Tibet [e.g., Bijwaard et al., 1998; Huang

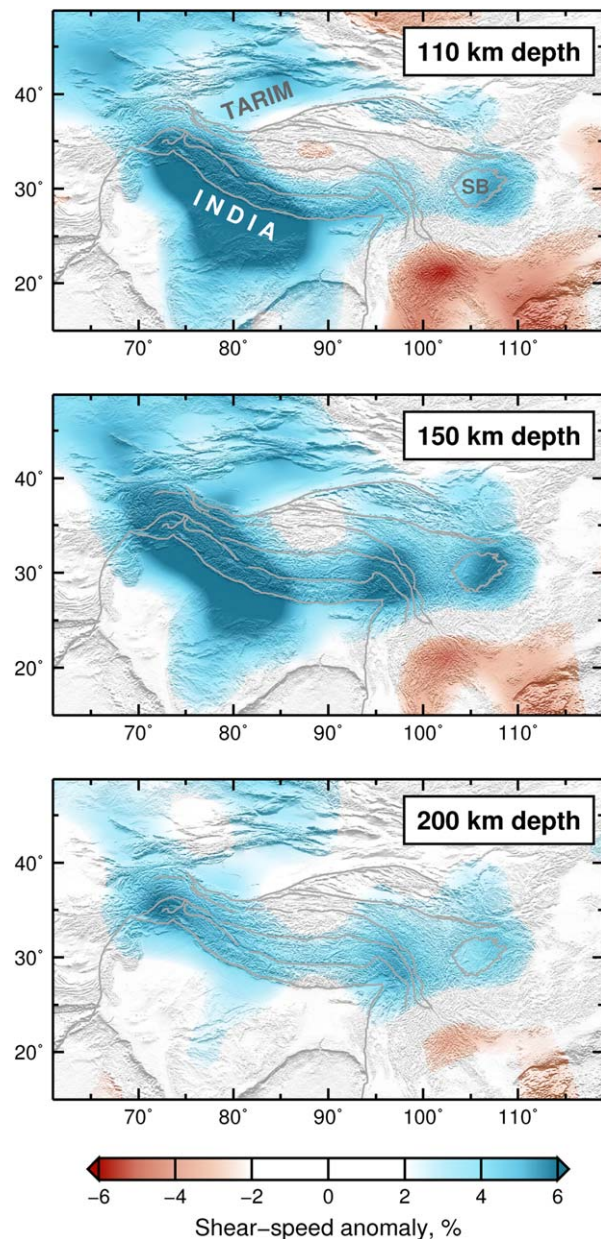


Figure 3. Shear-wave velocities beneath Tibet and surroundings according to the global tomographic model of Lebedev and van der Hilst [2008]. The reference S_1 -wave velocity values are, top to bottom, 4.38, 4.39, and 4.45 km/s, all at a reference period of 50 s. SB, Sichuan Basin.

and Zhao, 2006; Li et al., 2008; Replumaz et al., 2010a). This seeming absence of an anomaly due to subducted Indian lithosphere beneath central Tibet has motivated complex conceptual models with stacking of fragments of Indian lithosphere beneath the Himalaya and southernmost Tibet [Royden et al., 2008] or with lateral extrusion of the missing Indian lithosphere eastward [Replumaz et al., 2010b].



[11] The purpose of this study is to resolve the configuration of the Tibetan and Indian lithospheres beneath Tibet using robust V_S profiles constrained by new, highly accurate measurements of surface-wave phase velocities. The profiles are determined by nonlinear inversion of the broadband (up to 5–200 s) dispersion curves and resolve the crustal and upper-mantle structure from central to eastern and northeastern Tibet. The phase-velocity data require substantial high-velocity anomalies in the upper mantle beneath much of the plateau. Using integrated geophysical-petrological modeling, we show that large temperature anomalies are necessary to account for the observations and that they are consistent with the presence of subducted Indian lithosphere in the upper mantle beneath most of the plateau. The character of subduction, however, shows significant changes from west to east across Tibet.

2. Data and Measurements

[12] The fundamental advantage of interstation measurements of surface-wave phase velocities, compared to the “source-station” measurements normally used in large-scale tomography, is that they can be performed, with now available methods, in broader frequency bands [Meier *et al.*, 2004; Lebedev *et al.*, 2006]. This allows us to resolve trade-offs between model parameters in the crust and in the upper mantle and to determine seismic structure within both with higher accuracy, in particular for the amplitude of the anomalies.

[13] We chose 29 broadband-station pairs, formed by both permanent and temporary stations (PASSCAL (91/92) [Owens *et al.*, 1993], INDEPTH II and III [Nelson *et al.*, 1996; Huang *et al.*, 2000], HI-CLIMB [Nábelek *et al.*, 2009], and PASSCAL (Lehigh) [Sol *et al.*, 2007, Figure 1]. Each pair was chosen so that numerous suitable earthquake recordings were available for the measurements of interstation surface-wave dispersion, resulting in robust average phase-velocity curves.

2.1. Phase-Velocity Measurements

[14] Interstation phase-velocity measurements were performed in broad period ranges using a combination [Lebedev *et al.*, 2006] of cross correlation [Meier *et al.*, 2004] and the automated multimode inversion (AMI) of surface and S waveforms [Lebedev *et al.*, 2005]. The cross correlation of the vertical (transverse) components from

two stations aligned approximately along the same great-circle path with an earthquake (within 10°) measures the phase delay of Rayleigh (Love) waves. The fundamental-mode, interstation phase velocities are then calculated using the difference of the distances from the source to each of the two stations. The cross-correlation technique can measure accurate phase velocities for very broad period ranges, including the short periods (5–20 s) at which seismograms are often complex due to the diffraction of the surface-wave fundamental mode.

[15] At long periods, phase velocities can be difficult to extract using cross correlation because of the surface-wave interference with S and multiple S waves, especially for Love waves. They can be obtained, instead, using source-station, phase-velocity measurements derived from full waveform inversion with AMI. S , multiple S , and surface waves are simultaneously fit within a set of time-frequency windows, using synthetic seismograms generated by normal-mode summation. The fundamental-mode station-station dispersion curve can then be determined from a pair of source-station measurements (same event, two stations approximately on the same great-circle path), as a function of the differences between the source-station distances and between phase velocities for the two source-station pairs.

[16] The earthquakes contributing to our measurements are from both directions along the interstation paths, although predominantly from the east (from western Pacific and southeast Asia, Figures 4e–4h). The similarity of phase-velocity measurements calculated from earthquakes located on the opposite sides of the interstation paths is important, as systematic differences may indicate timing errors at the stations or measurement biases due to lateral heterogeneity between the source and the stations. For all the station pairs in our data set, the measurements from the different directions and different source regions are in mutual agreement (Figures 4i–4p), which confirms that they are unlikely to be biased by diffraction or mode interference.

[17] The fundamental-mode dispersion curves measured by cross correlation and AMI were combined, their consistency confirming their accuracy. Cross-correlation measurements are more numerous and dominate the averages along much of the curves, with the exception of long-period portions of some of the Love-wave curves (Figures 4s and 4t). Only smooth portions of each of the single-event curves were selected. Rough curves or



portions of curves and outliers were excluded. The selection of smooth curves reduces errors due to the diffraction of the fundamental mode [Pedersen, 2006] and due to the interference with higher modes, with the errors frequency-dependent and

thus, often associated with roughness of measured dispersion curves.

[18] The selection of smooth curves and the averaging over hundreds of measurements from

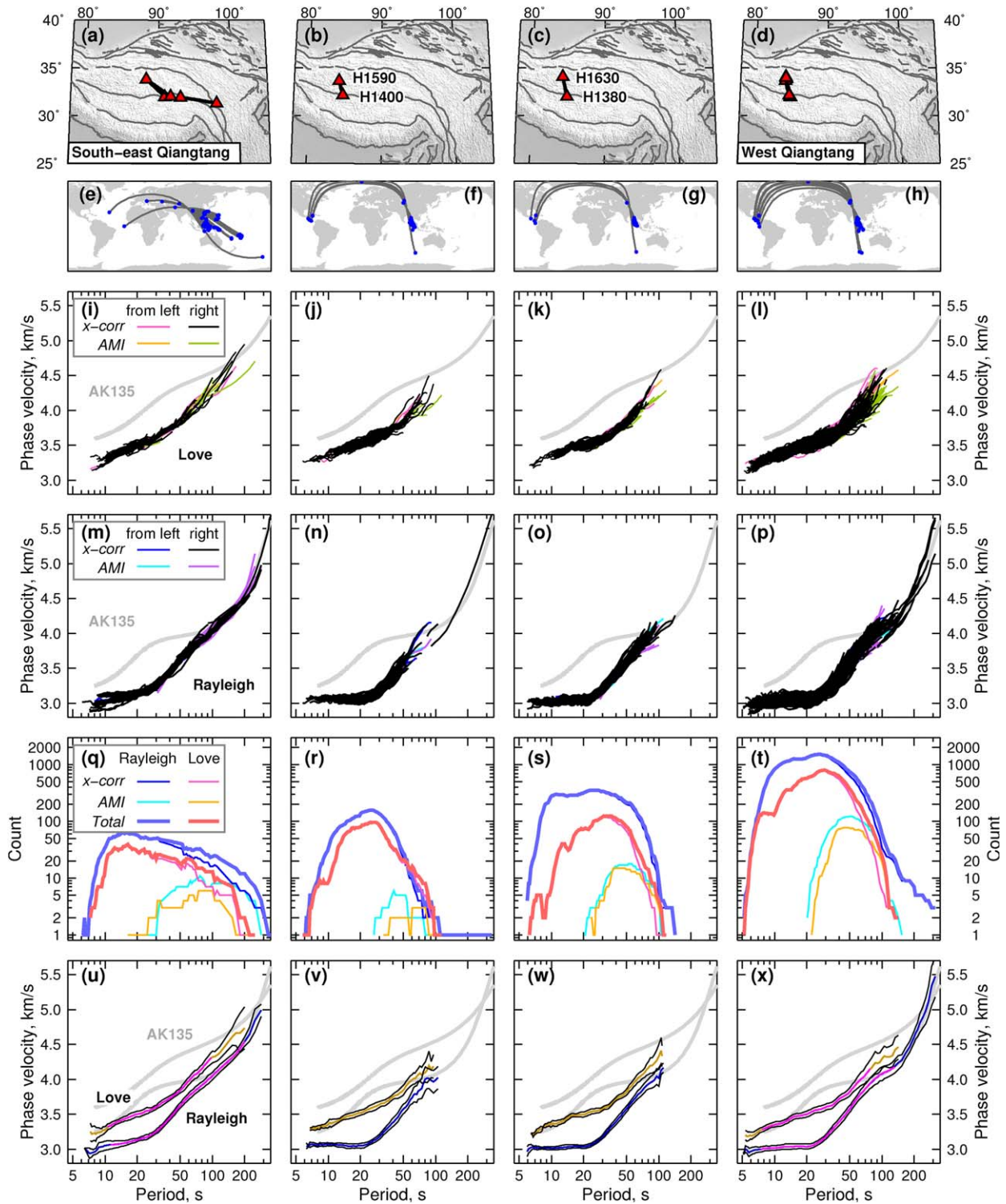


Figure 4.



earthquakes from different directions and distances result in highly accurate phase-velocity measurements. After the average phase velocity and its standard deviation were computed for each period, we selected only the smoothest parts of the average dispersion curves, with smallest standard deviations, for further processing (Figures 4u–4x).

2.2. Phase-Velocity Curves

[19] In the 7 to 50 s period range, both our Love- and Rayleigh-wave phase-velocity curves are well below the curves computed for the continental-average AK135 reference model [Kennett *et al.*, 1995], due to the very thick crust beneath Tibet [Romanowicz, 1982]. Our focus here is on longer-period surface waves, however, more sensitive to the deeper, mantle structure. We detect important systematic differences between dispersion curves from different parts of Tibet at periods longer than 40 s.

[20] Comparing our measurements, we find that neighboring station pairs show similar interstation dispersion curves. Station pairs H1400–H1590 and H1380–H1630 (Figures 4b and 4c), for example, are close to each other within western Qiangtang Terrane; as expected, they have very similar dispersion curves (Figures 4j–4k and 4n–4o). In addition to these two pairs, six other station pairs nearby (all from the northern part of the HICLIMB array) also show very similar dispersion curves. These measurements can thus be grouped together, to characterize the structure of this region within Tibet, west Qiangtang (Figure 4d). With hundreds of single-event Love- and Rayleigh-wave dispersion curves measured within this region (Figures 4l, 4p, and 4t), the average phase-velocity curves for it are robust in a broad period range for both Rayleigh and Love waves (Figure 4x). Similarly, three interstation pairs across

southeast Qiangtang are also grouped together (Figure 4a). Although the stations are relatively far apart, they yield very similar Rayleigh- and Love-wave dispersion curves (Figures 4i and 4m). Unlike in west Qiangtang, the interstation paths in southeast Qiangtang have different azimuths, so that the earthquakes contributing signal for the measurements are distributed in more diverse source regions around the globe (Figure 4e).

2.3. Regions Within Tibet

[21] Guided by the degree of similarity of phase-velocity curves, we identify seven regions within Tibet sampled by our measurements: west Lhasa, central Lhasa, west Qiangtang, southeast Qiangtang, east central Qiangtang, Songpan-Ganzi, and Qinling-Qilian. Figure 5a shows the grouped interstation pairs, indicating the location of each region. The dispersion curves from west Lhasa and Qinling-Qilian have the most distinctive curves when compared to the other regions across Tibet (Figure 5b). Between 10 and 50 s, phase velocities from the two paths sampling Qinling-Qilian orogen (region 7) are higher than from other paths (Figures 5b and 5h); this is due to the thinner crust in Qinling-Qilian, just outside of the high plateau. Within the high plateau (regions 1–6), Rayleigh and Love waves have very similar phase velocities in all regions between 10 and 40 s, with variations of less than 0.2 km/s (Figure 5b). Beyond 40 s, differences in the rates of phase-velocity increases with period in different regions indicate heterogeneity in the upper mantle.

[22] Within each region, phase-velocity differences between individual interstation pairs are mostly at short periods. The thin, pale-colored curves in Figures 5c–5h show the within-region velocity variations, most visible at 7–25 s. At very short periods these variations may be an effect of

Figure 4. Phase-velocity measurements for interstation pairs and for grouped regional averages. (a–d) The location of the stations (red triangles) and interstation paths (black lines). (e–h) The global maps show earthquakes (blue dots) and earthquake-station great-circle paths (black lines). (i–l, m–p) Love- and Rayleigh-wave dispersion curves are displayed in separate plots, each showing superimposed one-event measurements from different methods: cross correlation (*x*-corr) and automated multimode inversion (AMI). Different colors indicate the measurement method and wave-propagation direction. Grey curves show the dispersion curves computed for the AK135 reference model [Kennett *et al.*, 1995]. (q–t) The total number of measurements at each period for Love and Rayleigh waves is shown in red and blue, respectively, in the count graph. Different colors show the measurement count from different methods. (u–x) The resulting average dispersion curves for Love and Rayleigh waves and their standard deviations (black curves); pink indicates the most robust portions of the curves selected to be used in the inversions. The two columns in the middle illustrate interstation measurements for individual station pairs. The columns on the left and on the right show examples of region-average phase-velocity measurements, using all the data from all interstation pairs within the regions.

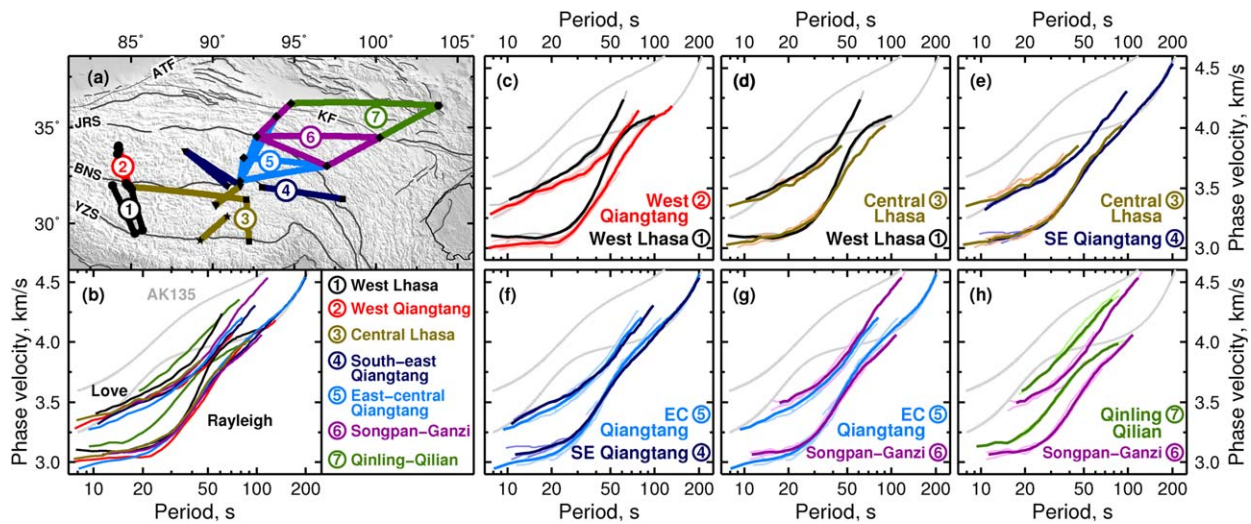


Figure 5. Broadband phase-velocity curves measured across Tibet. (a) Interstation paths within seven color-coded regions. Different symbols indicate stations of different networks as in Figure 1. (b) The seven Love-wave and seven Rayleigh-wave, region-average phase-velocity curves. Grey lines: Dispersion curves computed for the AK135 reference model [Kennett *et al.*, 1995]. (c–h) Comparisons of region-average dispersion curves. The color code is as in Figure 5a. Pale, thin curves are the phase-velocity measurements from individual interstation paths within the region; bold curves are region averages.

sediments; at intermediate periods (10–25 s) the anomalies are likely due to deeper crustal heterogeneity. Beyond 30 s, individual Rayleigh-wave measurements are remarkably consistent with each other within each region. Individual Love-wave interstation dispersion measurements tend to be noisier and form somewhat broader bundles. Bold, dark colored phase-velocity curves in Figure 5 are the averages over all the measurements from the station pairs within a region. These averages yield robust phase-velocity curves in period ranges broader than those of the curves for individual interstation pairs (pale curves) because they are computed from the larger number of all the “one-event” measurements from the region.

[23] A comparison of region-average curves at intermediate and long periods reveals strong lateral heterogeneity in the upper mantle beneath Tibet. The neighboring west Lhasa and west Qiangtang regions show the largest contrast in the Rayleigh-wave dispersion curves, with a sharp phase-velocity increase at periods above 30 s in west Lhasa indicating uppermost-mantle seismic velocities much higher than those beneath west Qiangtang (Figure 5c). Between 40 and 100 s, Rayleigh-wave phase velocities in central Lhasa are lower than in west Lhasa (Figure 5d) but higher than in Qiangtang (Figure 5e). The Rayleigh-wave phase velocities in both east central and southeast Qiangtang exceed the global reference values between 110 and 180 s.

3. Inversion

3.1. Inversion of Phase-Velocity Curves for Shear-Velocity Profiles

[24] We invert Rayleigh- and Love-wave dispersion curves simultaneously for a 1-D profile of the isotropic-average shear speed $V_S = V_{S(avg)} = (V_{SV} + V_{SH})/2$ and radial anisotropy $(V_{SV} - V_{SH})/2$, where V_{SV} and V_{SH} are the vertically and horizontally polarized shear speeds, respectively [Lebedev *et al.*, 2006; Endrun *et al.*, 2008]. The inversion is performed using a fully nonlinear, Levenberg-Marquardt gradient search. The search direction is computed at each iteration with the synthetic phase velocities computed directly from the V_{SH} and V_{SV} models, using a suitably fast version of the MINEOS modes code (Masters, <http://geodynamics.org/cig/software/mineos>). Compressional velocity V_P has a small but nonnegligible influence on the Rayleigh-wave phase velocity. V_P is assumed isotropic, and the ratio between the isotropic-average shear speed $V_{S(iso)}$ and V_P is kept fixed during the inversion. In the figures in this and following sections, we plot the Voigt isotropic-average $V_{S(iso)} = (2V_{SV} + V_{SH})/3$ instead of the arithmetic average $V_{S(avg)}$.

[25] Perturbations in the model are controlled by basis functions, boxcar-shaped in the crust and triangular in the mantle [Bartzsch *et al.*, 2011]. These define the sensitivity depth range of two

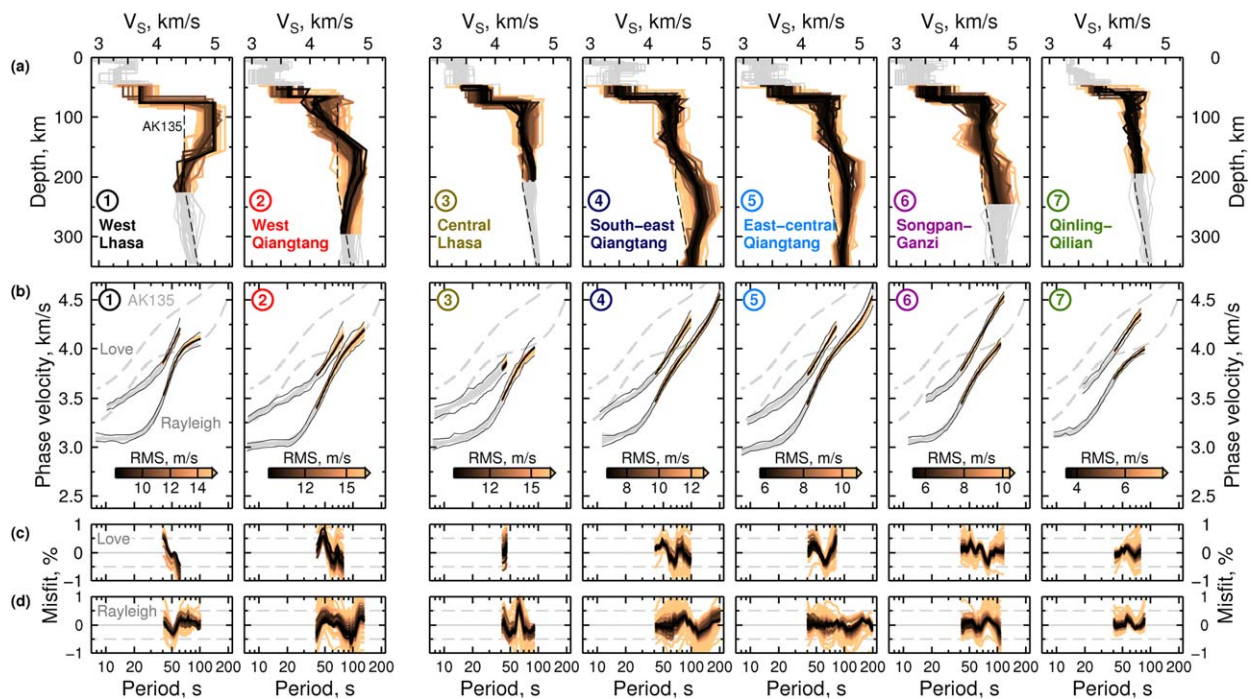


Figure 6. Shear-speed profiles for the seven regions within Tibet. (a) Each 1-D V_S profile is obtained in an independent, nonlinear, gradient-search inversion. (b) Synthetic phase velocities corresponding to the 1-D V_S profiles. (c, d) The data-synthetic misfit for the Love- and Rayleigh-wave phase velocity, respectively. The color scale indicates the data-synthetic RMS misfit for the combined Rayleigh- and Love-wave dispersion curves for periods >40 s. The colored depth ranges of the V_S profiles indicate the depth sensitivity for periods from 40 s up to the long-period cutoff for these data. All synthetic dispersion curves fit within the measured standard deviation (solid black curves). The standard errors of the measurements are much smaller than the standard deviations and would be similar to the line thickness on the plots; actual errors normally exceed standard errors, however, because of systematic errors in the data. Dashed lines are the AK135 reference model (Figure 6a) and synthetic phase-velocity curves computed for it (Figure 6b) [Kennett *et al.*, 1995].

independent inversion parameters: one for the perturbation in isotropic-average V_S and one for the amount of radial anisotropy. The depth of the Moho and three intracrustal discontinuities are additional inversion parameters. Slight norm damping is applied in order to avoid physically unrealistic models. All the V_S profiles are perturbed from the surface down to the shallow lower mantle, with the surface topography taken into account.

[26] The inversion results are fundamentally non-unique. Rather than selecting one preferred model, we obtain a suite of models that fit the data. The bundles of V_S profiles are generated in grid searches (section 3.2), complemented by the results of the targeted test inversions designed to answer specific questions, also discussed later. We plot the models for each region color-coded according to the data-synthetic fit they provide. In Figure 6, both the nonuniqueness of the models and their robust features are readily apparent. Although the entire dispersion curves were

inverted for crustal and mantle structure, the color of each profile and synthetic dispersion curve is determined by the phase-velocity, data-synthetic misfit computed over the frequency band most sensitive to the upper mantle ($T >40$ s). The colored depth ranges of the V_S profiles also indicate the depth sensitivity of the data (pale grey where not robust). The data-synthetic misfits for the Love and Rayleigh waves are shown in Figures 6c and 6d, respectively. The remaining misfits for the best fitting models (darkest lines) are due to noise in the data (given the broad depth ranges of phase-velocity sensitivity functions (supporting information Figure S1¹), sharp kinks in phase-velocity curves cannot be explained by any realistic structure). For most well-fitting models, the misfits are within $\pm 0.5\%$.

¹Additional supporting information may be found in the online version of this article.



3.2. Targeted Test Inversions and Parameter-Range Estimation

[27] Shear-velocity models yielded by inversions of phase-velocity curves are nonunique. In order to obtain definitive answers to specific questions regarding upper-mantle structure, we set up constrained inversions and in another approach, grid-search series of test inversions.

[28] To find profiles that fit both the surface-wave and other available data, information on the Moho depth and S_n velocity was included in the background models and fixed during the inversion (section 6.4). To delimit the ranges of shear speed and radial anisotropy consistent with the data, we performed grid-search series of test inversions, in which the parameter of interest was fixed at a value (incremented with a 0.025 km/s step for V_S ranges, for example) and the other parameters were allowed to vary freely. These grid-search/gradient-search inversions thus took into account the trade-offs between the parameter in question and all other parameters (Figures 6 and 7).

[29] For each model produced by an inversion, we calculate the data-synthetic RMS misfit for the combined Love and Rayleigh dispersion curves, for periods longer than 40 s. (In the tests targeting the deep anomaly beneath the Songpan-Ganzi region, we computed the misfit for periods >70 s, in order to reduce the influence of the shorter periods that are not sensitive to the depth range of interest.) As a criterion to identify acceptable models we allow for RMS values of up to 3.5 m/s above the best fitting model in the region. This threshold is higher than the formal standard error for most of our phase-velocity measurements. The standard errors—very small due to the very large number of measurements we average—would be unrealistic underestimates, however, because systematic measurement errors are not accounted for by a standard-error calculation assuming random errors only.

[30] Figure 7 shows examples of the results of grid-search series of test inversions. The average shear-velocity range in the upper ~ 70 km of the mantle beneath east central Qiangtang is determined in the tests shown in Figure 7a. Only the profiles near the boundaries of the acceptable range (found to be 4.32–4.54 km/s) are plotted, with well-fitting models in the middle of the range omitted for clarity. For each V_S model, corresponding Love- and Rayleigh-wave synthetic dispersion curves and data-synthetic misfits are

plotted in their respective frames. The tests performed to delimit the V_S range of a deep (175–225 km) high-velocity anomaly beneath east central Qiangtang are shown in Figure 7b; they constrain the S -velocity anomalies to be in the range of 4.7–11.8% above the global-average values. The V_S ranges were determined in this manner at different depths beneath each region and are listed in Table 1.

[31] The broadband Love- and Rayleigh-wave dispersion curves are also sensitive to the presence of radial anisotropy in the upper mantle. Beneath Songpan-Ganzi, for example (Figure 7c), an isotropic upper mantle would be inconsistent with the data and a minimum of 3.4% of radial anisotropy ($V_{SH} > V_{SV}$) is required.

4. Shear-Velocity Profiles

[32] The 1-D shear-velocity models for the seven subregions within Tibet (Figure 6) show strong lateral and depth variations in shear velocities across the plateau. In west Lhasa the data require very high isotropic-average shear velocities, close to 5 km/s, in an ~ 80 km thick layer in the upper mantle immediately beneath the Moho. In the adjacent west Qiangtang, in contrast, the average shear speeds in the uppermost ~ 80 km of the mantle are very low (4.18–4.33 km/s; Figure 6 and Table 1, regions 1 and 2). Below 150 km depth, west Lhasa shows no shear-velocity anomaly, whereas west Qiangtang is underlain by a 75 to 100 km thick high-velocity anomaly with V_S of 4.70–4.84 km/s. A similar configuration of a low- S -velocity layer in the uppermost mantle underlain by a high shear-velocity layer is found beneath central and south-eastern Qiangtang (regions 4 and 5), where the high-velocity feature is deeper (150 to 300 km depth). This high-velocity anomaly is also observed beneath eastern Songpan-Ganzi (region 6) below 150 km depth, but not beneath Qinling-Qilian (region 7). Uppermost-mantle S velocities in central and northeastern Tibet are relatively low, although not as low as those in west Qiangtang.

[33] Unlike west Lhasa, central Lhasa (region 3) shows no pronounced anomaly, with shear speeds only slightly faster than the global average. Similar, continental-average shear speeds are found in the shallow mantle to the north across the Kunlun Fault, beneath Qinling-Qilian, which also has a shallower Moho (~ 55 km depth; Figure 6, region 7).

[34] Radial anisotropy in the upper mantle beneath the Qiangtang Terrane, between the Moho and

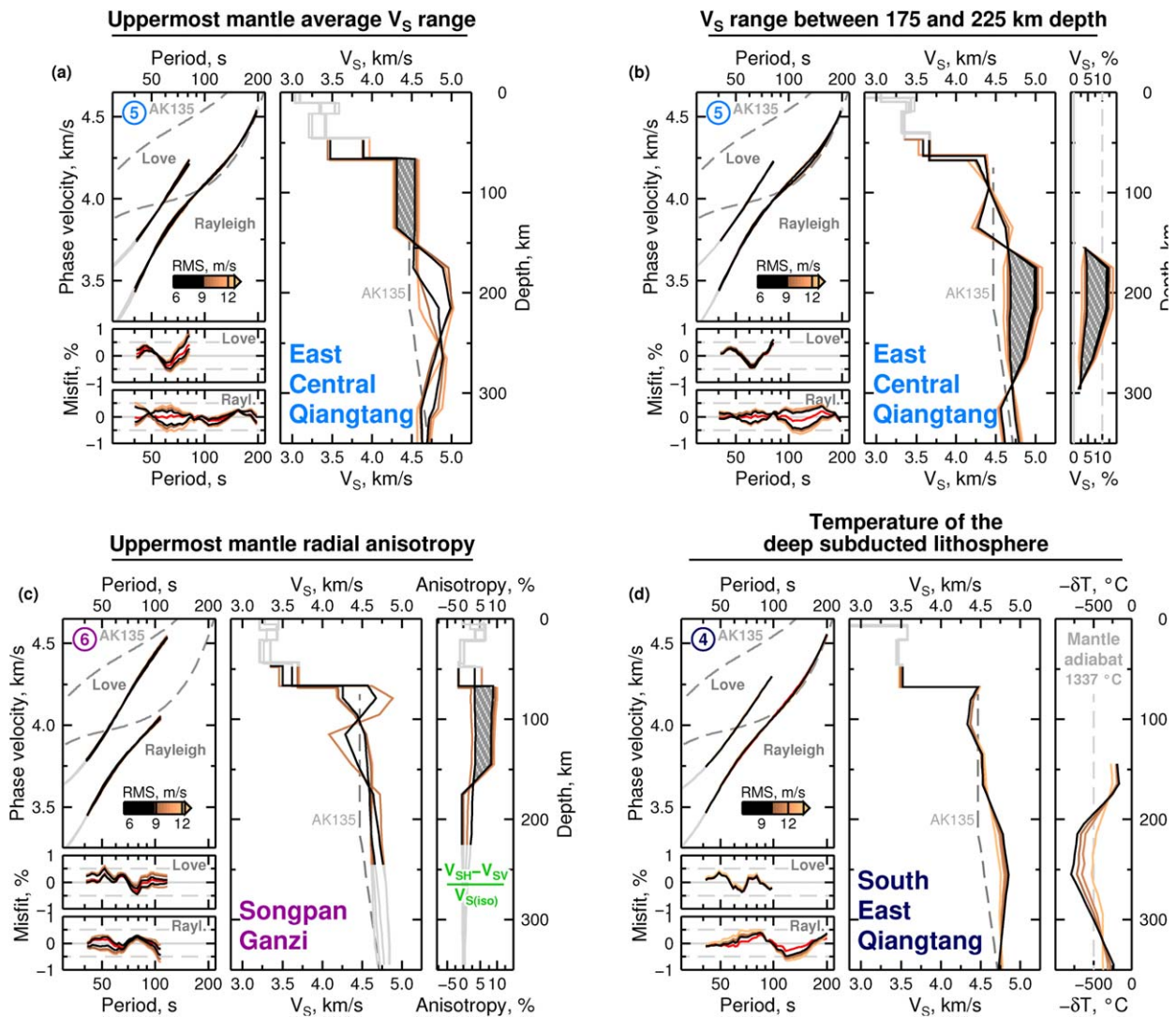


Figure 7. Four examples of the grid-search test inversions, performed to delimit V_S ranges, amounts of radial anisotropy, and temperature anomalies. The color scale indicates the data-synthetic RMS misfit of the combined Rayleigh- and Love-wave dispersion curves for periods >40 s. Black V_S profiles and the corresponding synthetic phase velocities are the upper and lower bound determined for the average V_S or radial anisotropy within the depth range tested. The RMS misfit given by models within the ranges is up to 3.5 m/s larger than the global minimum misfit. Red curves in the misfit frames are the data-synthetic misfits given by the best fitting profiles. (a) The tests for the uppermost-mantle-average V_S range beneath east central Qiangtang. (b) The tests for the V_S range between 175 and 225 km depths beneath east central Qiangtang; anomaly in percent relative to the AK135 reference is also shown. (c) The tests for uppermost-mantle radial anisotropy in the Songpan-Ganzi region. The isotropic Voigt average is computed as $V_{S(iso)} = (2V_{SV} + V_{SH})/3$. (d) The temperature anomaly beneath south-east Qiangtang. Temperature anomalies are relative to the mantle adiabat with T_p 1337°C (see Figure 8). Synthetic dispersion curves computed for AK135 [Kennett *et al.*, 1995] are shown with dashed lines.

150 km depth, is weak ($<2\%$ average), with isotropic models also fitting the data. In contrast, radial anisotropy is required by the data within the upper 80 km of the mantle beneath Songpan-Ganzi in the northeast of the plateau, with anisotropy in a 3.4–8.6% range. Qinling-Qilian, further northeast, also shows radial anisotropy, constrained to be in a 0.6–5.7% range between the Moho and 125 km depth.

5. Temperature Anomalies: Petrophysical Estimates

[35] Anomalously high S -wave velocities in the mantle are indicative of anomalously low temperatures. (Anomalies in mantle-rock composition also have an effect on S velocities but can account for an S -velocity increase of up to $\sim 1\%$ only [e.g.,



Table 1. Shear-Velocity and Temperature Anomalies in the Upper Mantle Beneath Tibet^a

Region	Region Number (Figure 5)	Uppermost Mantle		Subducted Lithosphere			Minimum Temperature Anomaly
		Depth Range (km)	Average V_S Range (km/s)	Depth Range (km)	V_S Range (km/s)	V_S Anomaly (%)	
West Qiangtang	2	Moho–115	4.18–4.33	150–200	4.70–4.84	5.1–8.3	–580
Southeast Qiangtang	4	Moho–135	4.26–4.45	215–265	4.82–5.10	6.6–12.9	–740
East central Qiangtang	5	Moho–135	4.32–4.54	175–225	4.68–5.00	4.7–11.8	–490
Songpan-Ganzi	6	Moho–135	4.32–4.53	185–235	4.63–4.88	3.2–8.9	–300
West Lhasa	1	Moho–155	4.87–5.01				
Central Lhasa	3	Moho–145	4.41–4.65				

^aTemperature anomalies are relative to a 1337°C mantle adiabat.

Schutt and Leshner, 2006.) Here we use integrated geophysical-petrological modeling to derive quantitative temperature estimates for the high-velocity anomalies in the upper mantle.

[36] First, we generate six synthetic geotherms defined by potential temperatures T_P ranging from 537 to 1337°C and use the LitMod modeling package [*Afonso et al., 2008; Fullea et al., 2009*] to calculate the corresponding profiles of shear velocity, density, and attenuation (Figure 8). LitMod combines petrological and geophysical modeling of the lithosphere and sublithospheric upper mantle and yields the physical properties of the mantle rock as a function of temperature, pressure, and bulk composition. Stable mineral assemblages and their physical properties are computed by Gibbs energy minimization (Perple_X) [*Connolly, 2005*]. Bulk

density and seismic velocities are calculated by averaging the mineral physical properties as described in *Afonso et al. [2008]* and *Fullea et al. [2009]*. Attenuation is taken into account [*Fullea et al., 2012*]. With decreasing temperature, the depths of the phase transformation from orthopyroxene to high-pressure Mg-rich clinopyroxene between 200 and 300 km [*Stixrude and Lithgow-Bertelloni, 2007*], of the dissolution of the pyroxene into garnet above the “410” discontinuity, and of olivines transformation into wadsleyite are seen rising to shallower depths in the V_S and density profiles (Figure 8). The mantle adiabats are approximately parallel, with the reference consistent with that of *Cobden et al. [2008]*.

[37] The families of the geotherms and corresponding V_S profiles (Figure 8) provide a mapping

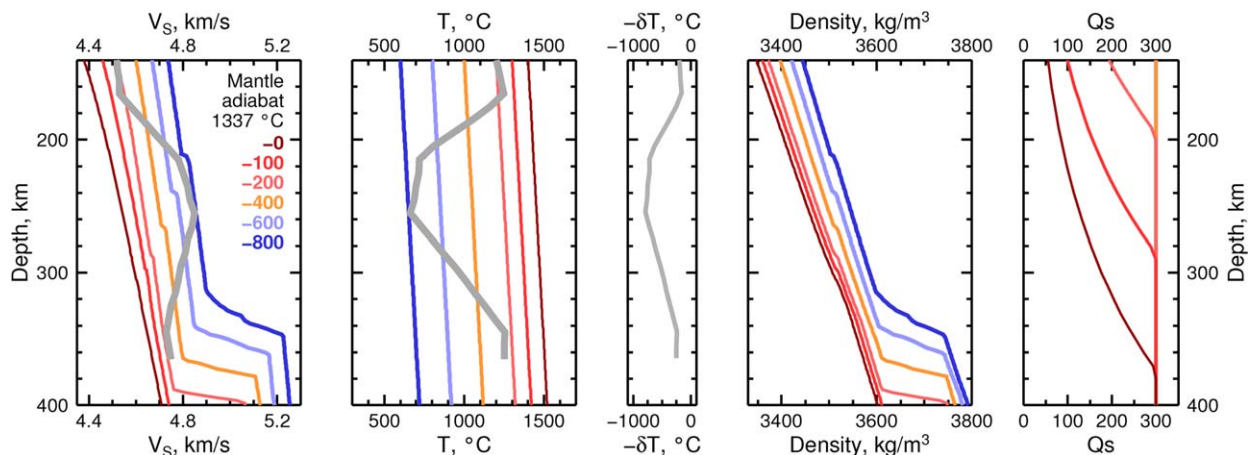


Figure 8. Estimation of temperature anomalies in the upper mantle. First, a set of reference 1-D models, each comprising the profiles of density, Q_s and V_S , is computed as a function of temperature, pressure, and bulk composition using LitMod [*Afonso et al., 2008; Fullea et al., 2009*]. The models are for a reference mantle adiabat with potential temperature T_P 1337°C (red) and for a series of temperature profiles that are cooler than the reference adiabat by the same amount at all depths, with the temperature decrease of up to 800°C (blue). An average mantle composition is assumed [e.g., *Fullea et al., 2012*]. The set of petrophysical models provides a mapping of shear velocities into temperature. Dark grey profiles: V_S for southeast Qiangtang (a conservative, well-fitting model, Figure 7d) and the estimated temperature profile and temperature anomaly.



of V_S into temperature. For a shear-velocity value that falls between two of the reference V_S profiles, temperature can be computed using interpolation between the two corresponding reference geotherms. We now select conservative 1-D V_S models (those with the deep shear-velocity anomaly at the lower bound of the range consistent with the data) and estimate the temperature anomalies with respect to the 1337°C adiabat (Figures 7d and 8). Temperatures within the deep high-velocity bodies beneath different parts of Qiangtang, for example, are estimated at 490–740°C below the 1337°C mantle adiabat (Table 1).

6. Discussion

[38] The upper mantle beneath the Tibetan Plateau is strongly heterogeneous. Some of the major features of this heterogeneity, such as the strong contrast at 100 to 150 km depth between the high shear-wave speeds in southwestern Tibet and low shear-wave speeds in central Tibet (this contrast is across the BNS near the longitude 85°E and is the difference between our west Lhasa and west Qiangtang regions), are also resolved by tomographic models (Figure 3, 110 km depth). The amplitudes of the anomalies, however (and, thus, the absolute shear-wave velocities beneath Tibet), are determined more accurately by the robust profiles constrained by broadband surface-wave dispersion. In the deeper upper mantle, the prominent high-velocity anomaly around 200 km depth is not resolved by many body-wave models, whereas surface-wave models that do resolve it have been uncertain regarding its depth range and especially, the amplitude. Our profiles (Figure 6) constrain the ranges of shear-speed values consistent with the dispersion data and enable quantitative estimation of the associated temperature anomalies, with important inferences on the configuration of the subducted lithosphere beneath Tibet and the mechanisms of the India-Asia convergence.

6.1. Underthrusting of India Beneath West Lhasa

[39] In west Lhasa, the average shear velocity between the Moho and 155 km depth is 4.87–5.01 km/s (Figure 6 and Table 1, region 1). These values are very high, higher than within the lithospheres of cratons (Figure 9a, *Lebedev et al.* [2009]), thought to be the thickest and coldest lithospheres on Earth. Very high seismic velocities beneath southwest Tibet have previously been

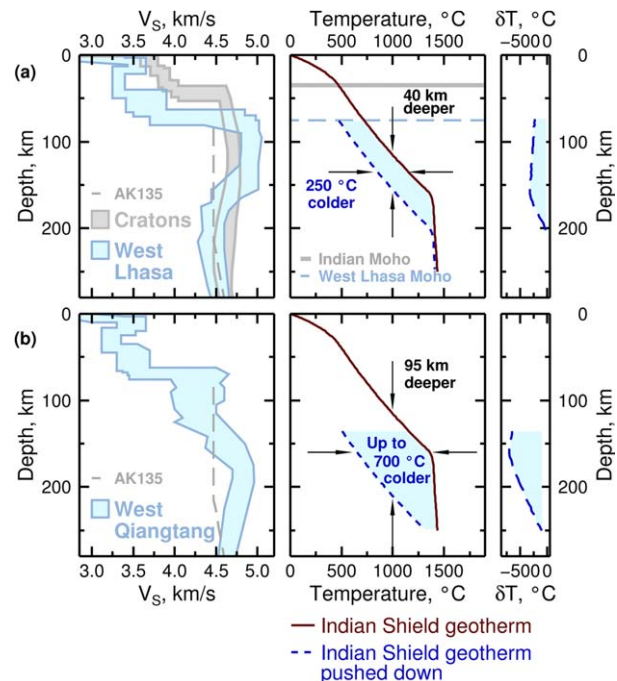


Figure 9. The thermal origin of high-velocity anomalies beneath the west Lhasa and west Qiangtang regions. (a, left) The S -velocity profile range for west Lhasa, with an average Moho at 75 km depth (light blue), and the S -velocity profile range for cratons globally, with an average Moho depth at 35 km (light grey) [*Lebedev et al.*, 2009]. (a, centre) The Indian Shield geotherm (bold solid line) [*Priestley et al.*, 2008], and the same geotherm pushed down by 40 km (dashed line); 40 km is an estimate of how much the Indian lower crust and mantle lithosphere need to go down to underthrust the Himalayas and western Lhasa, with the upper crust removed. (a, right) The estimated temperature anomaly at depth. (b) Same as Figure 9a, but for west Qiangtang, with the Indian Shield geotherm shifted 95 km down.

reported [e.g. *Oreshin et al.*, 2008; *Hanna and Weeraratne*, 2013].

[40] The extreme seismic-velocity (and therefore, thermal) anomaly beneath west Lhasa can be explained by the underthrusting of the cratonic Indian lithosphere beneath the thick Tibetan crust. The underthrusting implies that the cold lithosphere has sunk by a few tens of kilometers. This, in turn, means that it has become more thermally anomalous at the depth that it now is at.

[41] A simple temperature estimate for the underthrust Indian lithosphere can be obtained by shifting the geotherm of the stable Indian Shield, now south of the Himalayas [*Priestley et al.*, 2008], down to a greater depth. For this estimate, we assume that the Indian lithosphere now beneath western Lhasa had, prior to the underthrusting, a geotherm similar to that beneath India today. We



also neglect the modest heating [e.g., Deal *et al.*, 1999] that it has undergone in the few million years since plunging under the Himalayas and sliding below Tibet. (Estimating that the southern and northern boundaries of Lhasa near 85°E are about 250 and 500 km, respectively, north of the Himalaya front, taking a convergence rate here of 3.8 cm/yr [Hatzfeld and Molnar, 2010], and neglecting internal deformation of the (probably, stiff) cratonic lithosphere, we can estimate that the Indian lithosphere now under west Lhasa has been underthrust beneath the Himalayas and Tibet for around 10 Myr, on average.) The Moho beneath west Lhasa is likely to be the Indian Moho [Nábelek *et al.*, 2009] and is at about 75 km depth, 40 km deeper than the Indian Moho south of the Himalayas (~35 km depth) [e.g., Gupta *et al.*, 2003; Rai *et al.*, 2003]. Moving the shield geotherm down by 40 km, we can thus estimate that the underthrust Indian lithosphere should be ~250°C colder relative to the (already cold) Indian lithosphere south of Himalayas at the same depth (Figure 9a). This can account for the extremely high seismic velocities that we detect beneath western Lhasa.

[42] In west central Tibet near longitude 85°E—the location of the HI-CLIMB profile—India underthrusts Tibet as far north as the BNS. Farther north along 85°E, the Indian lithosphere is no longer present in the uppermost mantle, as evidenced by a sharp shear-velocity decrease from west Lhasa to west Qiangtang in the upper 100 km of the mantle shown by our profiles. This result is consistent with the published interpretation of HI-CLIMB results [Nábelek *et al.*, 2009] and also, with the lateral extent of high-velocity anomalies in both surface-wave and body-wave tomographic models [Lebedev and van der Hilst, 2008; Li *et al.*, 2008].

[43] In western Tibet, west of longitude 85°E, surface- and body-wave tomographic models show a high-velocity anomaly in the uppermost mantle similar in amplitude to that beneath Lhasa at 85°E and extending farther north, up to the Tarim Basin (Figure 3). This suggests that cratonic Indian lithosphere underthrusts Tibetan crust across the western and southwestern parts of the plateau (the areas underlain by the prominent high-velocity anomalies, Figure 3) [Lebedev and van der Hilst, 2008; Li *et al.*, 2008]. Interestingly, the NW–SE trending northern boundary of the high-velocity lithospheric mantle—likely to indicate the mechanically strong Indian lithosphere underthrusting the Tibetan crust—roughly coincides

with the trace of the Karakoram Fault at the surface [Klemperer *et al.*, 2013], suggesting a possible lithospheric-mantle control on the localization of deformation on this fault.

[44] Although the Indian lithosphere must underthrust the central part of the Himalayas just as it underthrusts their western part, central Lhasa does not display a high-velocity anomaly in the uppermost mantle seen in western Lhasa. Our profiles confirm this difference, seen previously in tomographic images (Figure 3), and indicate that average S velocities across central Lhasa are close to the continental average (Figure 6 and Table 1, region 3). This suggests that the Indian lithosphere consumed recently beneath this part of the Himalayas was warmer and thinner compared to that in the west. The global-average seismic velocities in the lithospheric-mantle depth range would also be consistent with a relatively warm and thin Indian lithosphere sliding beneath a thin mantle lithosphere of central Lhasa itself. Radial and lateral small-scale heterogeneities, if present, could be averaged in the region-average profiles [Liang *et al.*, 2012], showing the normal average V_S in this part of Lhasa.

6.2. Subducted Indian Lithosphere Beneath Central and Eastern Tibet

[45] High-velocity anomalies at around 200 km depth are seen beneath much of Tibet in most tomographic models constrained with surface waves or multimode surface waves [Griot *et al.*, 1998; Shapiro and Ritzwoller, 2002; Friederich, 2003; Priestley *et al.*, 2006; Kustowski *et al.*, 2008; Lebedev and van der Hilst, 2008; Panning *et al.*, 2012] (Figure 3). Moreover, most of the tomographic models show a continuous anomaly dipping from south to north beneath southern Tibet and flattening further north, consistent with the high velocities being due to the subducted Indian lithosphere.

[46] Compared to the large-scale tomography, our shear-velocity profiles yield more accurate values of the amplitude and depth range of the anomalies in the 120 to 300 km depth interval. Petrophysical estimates of the temperature within the high-velocity feature indicate that it is a few hundred degrees Celsius colder than the normal asthenosphere (Table 1), consistent with it being the subducted, thick continental lithosphere of India. An intuitively clear estimate of the temperature expected within subducted Indian lithosphere is given by shifting the estimated geotherm of the



(unsubducted) Indian Shield south of the Himalayas down to the depth of the high-velocity anomalies. For west Qiangtang, for example, this gives a predicted thermal anomaly of 700°C (Figure 9). Our independent, petrophysical estimation of the temperature anomaly directly from V_S yields similar values (at least 580°C).

[47] The entire high-velocity body resolved by surface-wave and multimode-surface-wave tomographic models at around 200 km beneath Tibet (Figure 3) is thus likely to represent subducted Indian lithosphere. An alternative previous interpretation of the high-velocity anomaly attributed it to the deep portion of the Tibetan lithosphere, thickened by the continental collision [McKenzie and Priestley, 2008]. This interpretation, however, would be difficult to reconcile with our data that require a thick (70–80 km) layer of low seismic velocities in the upper mantle just below the Moho, most readily interpreted as the warm Tibetan lithosphere and asthenosphere. McKenzie and Priestley [2008] argued that radioactive heating from the thick Tibetan crust could heat up the uppermost-mantle portion of an otherwise cold, thick lithosphere beneath it. In their model, seismic velocity in the uppermost mantle decreased with time due to the heating. Even after a very long heating time of 90 Myr, however, the predicted V_S was over 4.5 km/s below the Moho and increased to around 4.6 km/s at 100 km depth. These values are inconsistent with the surface-wave dispersion observations, which require much lower velocities in the upper few tens of kilometers of the mantle (Figures 6 and 10).

[48] Another model of the lithospheric evolution beneath Tibet invokes convective removal of the thickened mantle lithosphere or of its lower portion [Houseman et al., 1981; Molnar et al., 1993; Hatzfeld and Molnar, 2010]. Sinking drips of cold lithospheric rock could produce substantial high-velocity anomalies in the mantle, and it is probable that such dripping has occurred as Tibetan lithosphere was shortened in the course of the India-Asia collision. However, the lateral extent of the high-velocity anomalies at 150 to 250 km depths beneath Tibet is vast, and they are unlikely to represent a single chunk of lithospheric material delaminated from the bottom of Tibetan lithosphere recently. Accumulation of smaller drips at 150 to 250 km depths could be another possibility, but there is no evidence for a sufficiently strong viscosity or density contrast at 250 to 300 km depths to prevent the large volume of cold material from sinking deeper into the mantle [Hatzfeld and

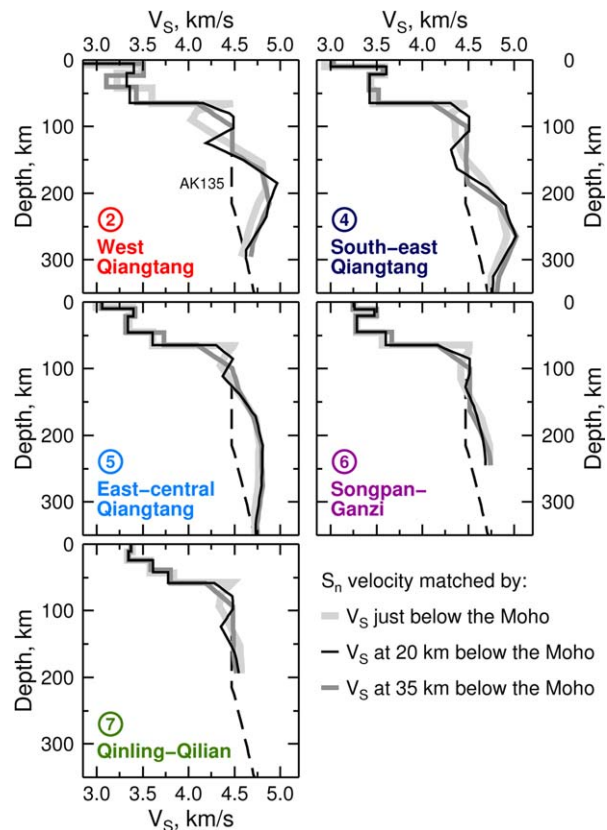


Figure 10. Example V_S profiles for northern Tibet that fit the surface-wave data and the published Moho depths and S_n velocities. S_n velocity is constrained to match at Moho depth (light grey), at 20 km below the Moho (black), and at 35 km below the Moho (dark grey). The depth extent of the profiles varies according to the sensitivity (frequency band) of phase-velocity curves for the regions. Dashed line is the AK135 reference model [Kennett et al., 1995].

Molnar, 2010]. We thus conclude that the high-velocity (low-temperature) anomalies at 150 to 250 km depths are unlikely to be only, or mostly, due to the lithospheric drips, even though the interaction of sinking plumes of cold lithospheric rock with the subducting Indian lithosphere beneath them is likely and may be an interesting feature of Tibetan upper-mantle dynamics.

[49] In contrast to surface-wave tomographic models, many models constrained with teleseismic P -wave travel times do not show any high-velocity anomalies at 150–300 km beneath central, northern, and eastern Tibet [e.g., Bijwaard et al., 1998; Huang and Zhao, 2006; Li et al., 2008; Replumaz et al., 2010a]. As discussed by Li et al. [2008], the discrepancy may be due to differences in data sampling, with teleseismic body waves, in particular, arriving to stations at steep angles and providing better lateral than radial resolution. This can



be verified by further analysis in the future, for example, by joint inversion of surface-wave and teleseismic body-wave data or by incorporation of surface-wave-constrained models of Tibetan crust in the reference models for teleseismic tomography.

[50] We conclude that high- S -velocity anomalies in the 120 to 300 km depth range beneath the

Qiangtang Terrane and the eastern Songpan-Ganzi Terrane are likely to indicate cold, subducted Indian lithosphere. The $+2.5\%$ V_S anomaly contour line (Figure 11b) given by surface-wave tomography at 200 km depth (Figure 3) may thus show, approximately, the northern extent of the subducted Indian lithosphere that is now in the upper mantle beneath Tibet (Figure 12, eastern profile). The inversions of broadband dispersion curves performed in this study confirm the occurrence of the anomaly, establish more accurately its amplitude and depth range, and show that the large corresponding temperature anomaly is consistent with that expected within subducted Indian lithosphere.

6.3. Subducted Indian Lithosphere-Asthenosphere Boundary

[51] The LAB can be identified as the depth of the reduction in V_S near the bottom of the lithosphere. Such V_S decrease at the bottom of the Indian lithosphere, underthrust and subducted beneath Tibet, is evident in a number of our profiles. In western Lhasa the LAB is seen as the V_S reduction at 150 to 200 km depths (Figure 6, region 1). The subducted Indian lithosphere beneath west Qiangtang, seen in the profiles as a deeper high-velocity layer, bottoms at around 250 km depth (region 2), and the similar anomaly beneath eastern and northeastern Tibet bottoms at around 300 km (regions 4–6).

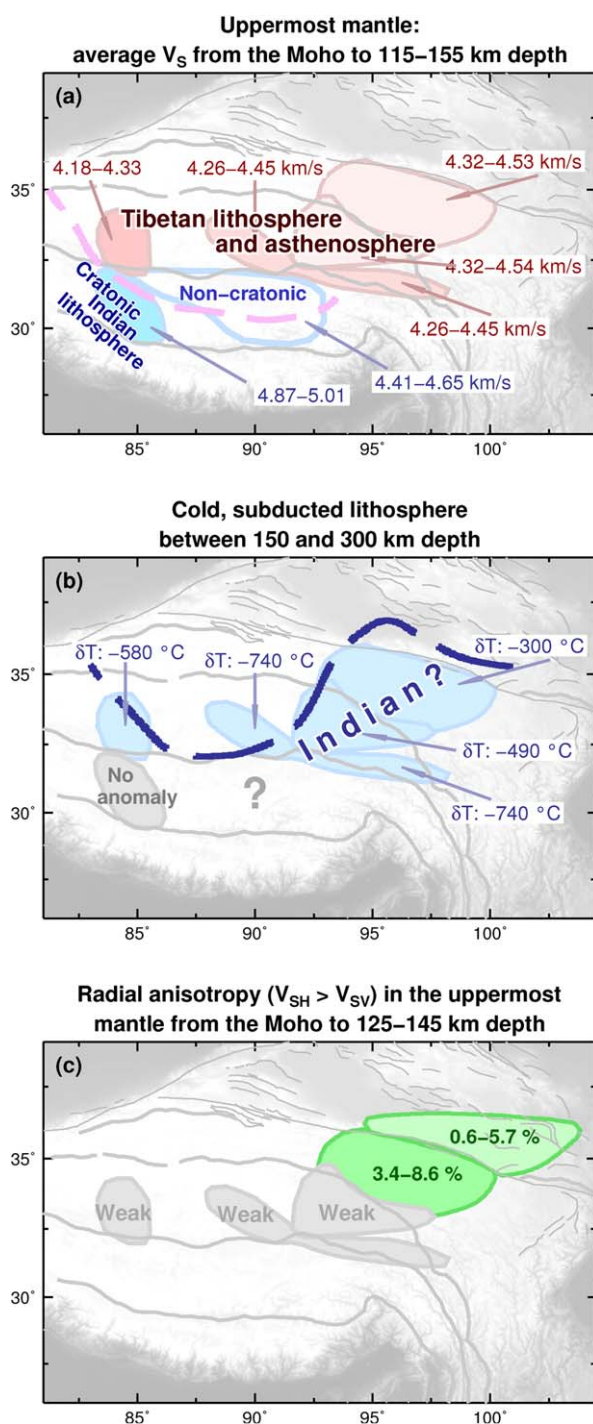


Figure 11. Shear-speed distributions, temperatures, and radial anisotropy in the upper mantle beneath Tibet. Shaded areas indicate the regions within Tibet for which the values were derived. (a) Uppermost-mantle-average V_S ranges constrained in this study. The depth ranges for which the averages are determined sample the Indian cratonic lithosphere in the west Lhasa and the Tibetan lithosphere and asthenosphere in central, northern, and eastern Tibet. Specifically, the depth ranges extend from the Moho down to 115 km (west Qiangtang), 135 km (east central Qiangtang, southeast Qiangtang, and Songpan-Ganzi), 145 km (central Lhasa), and 155 km (west Lhasa) (Table 1). Dashed, bold pink line: the approximate northern boundary of the high-velocity anomaly (interpreted as the Indian lithosphere) beneath western and southern Tibet at 110 km depth in the global tomographic model of *Lebedev and van der Hilst* [2008] (Figure 3). (b) Temperatures within the anomalously cold body at 150 to 300 km depth in the upper mantle, which we interpret to be the subducted Indian lithosphere. Thick, dashed blue line is a $+2.5\%$ anomaly contour at 200 km depth beneath Tibet from the global surface-wave tomography (Figure 3). (c) Uppermost-mantle radial anisotropy in northeastern Tibet, in the depth ranges from the Moho to 125 km depth (Qinling-Qilian) and from the Moho to 145 km depth (Songpan-Ganzi).

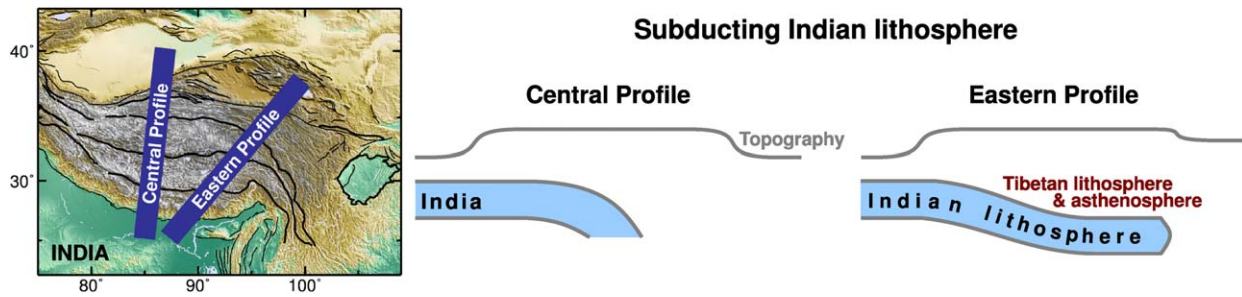


Figure 12. The complex subduction of Indian lithosphere beneath Tibet. (left) Elevation map of Tibet and the locations of the central and eastern profiles. (right) The underthrusting and steep-angle subduction of India beneath west central Tibet and the shallow-angle subduction of India beneath eastern Tibet.

[52] These estimates of the subducted Indian LAB depths show an encouraging agreement with those obtained from receiver functions, a data type with sensitivity to discontinuities in seismic velocities at depth. *Zhao et al.* [2010] mapped the Indian LAB using S receiver functions measured along N–S and NE–SW corridors in western, central, and eastern Tibet. In western Tibet, they detected a horizontal converter at around 210 km depth, roughly consistent with the bottom of the high-velocity lithosphere seen in our profile for west Lhasa. In central Tibet, S receiver functions showed an interface dipping northward, from 120 to 130 km depth beneath the Himalayas to 200 km depth near the BNS. It was interpreted as the bottom of the subducting Indian lithosphere [*Zhao et al.*, 2010]. If extrapolated north of the BNS, to beneath central and eastern Qiangtang and Songpan-Ganzi, this interface will reach the 250 to 300 km depth range, consistent with our results for these regions. Receiver functions may thus provide independent and complementary evidence on India's shallow-angle subduction beneath Tibet (although we have to keep in mind that substantial disagreements between different receiver-function results have been reported).

6.4. Tibetan Lithosphere and Asthenosphere

[53] Shear-wave velocities in the top few tens of kilometers of the mantle are particularly low beneath the west Qiangtang region (4.18–4.33 km/s, Table 1, region 2) and are closer to continental averages in the east of the plateau. Although we do detect high-velocity layers at greater depth beneath central and eastern Tibet, they are at 50–80 km below the Moho, making it unlikely that they represent the lower parts of a very thick lithosphere. Instead, the high velocities at 150 to 250

km depths probably indicate the subducted Indian lithosphere, and the layer with low-to-average shear velocities between the Moho and 120 to 150 km depth contains the warm Tibetan lithosphere and asthenosphere. Radioactive heating from the thick Tibetan crust [*McKenzie and Priestley*, 2008] is likely to have contributed to the high temperatures and relatively low seismic velocities within the thin Tibetan mantle lithosphere. Evidence for an S -velocity increase at the top of the subducted Indian lithosphere below may have been seen in S -to- P conversions [*Wittlinger et al.*, 2004].

[54] Our phase-velocity measurements put tight constraints on the average V_S in the depth range comprising the Tibetan lithosphere and asthenosphere. Finer structure within this layer, however, is difficult to resolve with surface-wave data alone, due to the nonuniqueness of the models constrained by the data. Important additional information is given by published studies of the distributions of the S_n and P_n wave speeds, efficiency of S_n propagation, and the frequency dependence of these waves' propagation.

[55] S_n tomography shows low-to-average S_n velocities in northern Tibet, with minimum wave speeds ranging from 4.33 [*Ritzwoller et al.*, 2002] to 4.45 [*Sun et al.*, 2008a, 2008b] and 4.47 km/s [*Pei et al.*, 2007]. Low-frequency S_n waves (0.2–1.0 Hz) have been observed to propagate efficiently across the northern part of the plateau with a velocity of ~ 4.7 km/s [*Barron and Priestley*, 2009]. At higher frequencies (>1 Hz), S_n propagates inefficiently through much of northern Tibet [*Barazangi and Ni*, 1982; *McNamara et al.*, 1995; *Barron and Priestley*, 2009].

[56] P_n velocities north of the BNS are close to continental averages, at about 8.0 km/s [*McNamara et al.*, 1997; *Hearn et al.*, 2004; *Liang et al.*,



2004; Meissner *et al.*, 2004; Phillips *et al.*, 2005; Liang and Song, 2006; Sun and Toksöz, 2006; Pei *et al.*, 2007]. Hearn *et al.* [2004] distinguished P_n velocities within the upper and lower lid and concluded that uppermost-mantle P -wave velocity increased with depth.

[57] In order to reconcile surface-wave and S_n observations quantitatively, we performed inversions of surface-wave data with S_n constraints. The Moho depths were fixed at values from receiver-function studies [Kind *et al.*, 2002; Kumar *et al.*, 2006; Tseng *et al.*, 2009; Nábelek *et al.*, 2009; Yue *et al.*, 2012] and deep seismic sounding [Zhao *et al.*, 2001; Zhang and Klemperer, 2005; Liu *et al.*, 2006; Li *et al.*, 2006]. Because of the ambiguity regarding the depth that S_n samples, we performed a series of different inversions, fixing shear-wave speed at the S_n velocity value [Ritzwoller *et al.*, 2002; Sun and Toksöz, 2006; Sun *et al.*, 2008a, 2008b] at different depths in the upper mantle, from just below the Moho to 20–35 km below the Moho. Figure 10 shows three different V_S models for each of our regions in northern Tibet. Each of the models fits the data well. Together, they display the range of possible uppermost-mantle structures in northern Tibet consistent with surface-wave and other observations.

6.5. Radial Anisotropy in the Shallow Mantle

[58] Radial anisotropy, the difference between the horizontally and vertically polarized shear speeds, can yield important information on finite strain and flow within the mantle and crustal rock. The strength of radial anisotropy in the upper 100–150 km of the mantle varies across Tibet, with weak or no radial anisotropy across the Qiangtang Terrane and strong anisotropy ($V_{SH} > V_{SV}$) beneath Songpan-Ganzi (Figure 11c).

[59] Interestingly, this pattern is nearly the opposite of that observed in the mid-lower crust, where radial anisotropy is strong in western and central Tibet and weak or absent in eastern Tibet [Shapiro *et al.*, 2004; Agius, 2013]. Shapiro *et al.* [2004] showed that strong radial anisotropy in the mid-lower crust correlated with locations of normal faults and was probably due to the alignment of mica crystals by the flow associated with crustal thinning. In eastern Tibet, where upper-crustal deformation is primarily on strike-slip faults and no crustal thinning is apparent, radial anisotropy in the mid-lower crust is weak or absent. Although

anisotropy in the upper mantle has a different source—it is due to the alignment of olivine rather than mica crystals—the differences in lateral variations of radial anisotropy in the crust and the mantle point to differences in the distributions of deformation patterns at different depths. Strong anisotropy beneath Songpan-Ganzi, in particular, may reflect flow in Tibetan asthenosphere [e.g., Zhang *et al.*, 2011; Leon Soto *et al.*, 2012] above the subducted Indian lithospheric slab; anisotropy within the Tibetan mantle lithosphere there can also account for the observations. Layering of radial and azimuthal anisotropy and of crustal and mantle deformation [Agius, 2013] will be investigated in detail in a future publication.

7. Conclusions

[60] Prominent high-velocity anomalies beneath Tibet are consistent with the presence of underthrust and subducted Indian lithosphere beneath much of the plateau (Figure 12). The very high shear-wave speeds within the mantle lithosphere beneath southwestern Tibet may reach 5 km/s, well above the highest values in stable continental lithosphere globally (i.e., beneath stable cratons). These high shear speeds are due to the underthrusting of the cold Indian lithosphere beneath the thick Tibetan crust, with the associated submergence of the lithosphere (and its geotherm) by an estimated 40 km giving rise to a $\sim 250^\circ\text{C}$ extra low-temperature anomaly within it.

[61] Beneath central, eastern, and northeastern Tibet, pronounced high-velocity anomalies are required by the data in 120 to 250 km (west central Qiangtang) and 150 to 300 km (eastern Qiangtang and Songpan-Ganzi) depth ranges. Estimated negative temperature anomaly within this high-velocity body is at least 500°C , on average, consistent with it being the subducted Indian lithosphere. Recent surface-wave tomography and receiver-function studies show a high-velocity layer (likely to be the Indian lithosphere) and a discontinuity (likely the Indian LAB) dipping northward at a shallow angle from the Himalaya toward northeastern Tibet, consistent with our interpretation.

[62] In contrast to western and southwestern Tibet, where the mantle lithosphere (and, possibly, lower crust) are those of the underthrusting Indian Plate, central and eastern Tibet are underlain by warm, Tibetan mantle lithosphere and asthenosphere. The S -velocity averages over the depth interval



from the Moho to 120–150 km vary laterally in the 4.18 to 4.54 km/s range; the mantle lithosphere and shallow asthenosphere within this depth interval are thus characterized by relatively high temperatures.

[63] Surface-wave measurements are easily reconciled with published Moho depths and S_n wave velocities. Models with shear velocities matching S_n values just below the Moho and at a 20 or 35 km depth below the Moho can all fit surface-wave data.

[64] Radial anisotropy in the Tibetan mantle lithosphere and asthenosphere is weak beneath the Qiangtang Terrane but strong beneath eastern Songpan-Ganzi ($>3.4\%$, with $V_{SH} > V_{SV}$); it is also required by the data beneath Qinling-Qilian. Interestingly, this pattern is nearly the opposite of that detected previously in the lower crust (strong anisotropy beneath western and central Tibet, none beneath NE Tibet) [Shapiro *et al.*, 2004], which must reflect differences in deformation and flow patterns in the crust and upper mantle. In the mantle, anisotropy beneath eastern Tibet is probably related to the asthenospheric flow above the subducting Indian slab.

Acknowledgments

[65] We are grateful to two anonymous reviewers for detailed, constructive comments and suggestions that helped us to improve this manuscript. We thank Jan Vozar and Javier Fullera for their assistance in petrophysical modeling. The facilities of the IRIS Data Management System (IRIS Data Management Center) were used for access to waveform and metadata used in this study. Figures were made using Generic Mapping Tools (GMT) software [Wessel and Smith, 1998]. This study was supported by Science Foundation Ireland (grants 08/RFP/GEO1704 and 09/RFP/GEO2550).

References

- Afonso, J. C., M. Fernández, G. Ranalli, W. L. Griffin, and J. A. D. Connolly (2008), Integrated geophysical-petrological modeling of the lithosphere and sublithospheric upper mantle: Methodology and applications, *Geochem. Geophys. Geosyst.*, 9, Q05008, doi:10.1029/2007GC001834.
- Agius, M. R. (2013), The structure and dynamics of the lithosphere beneath Tibet from seismic surface-wave analysis, PhD thesis, Trinity College Dublin, Ireland.
- Aitchison, J. C., J. R. Ali, and A. M. Davis (2007), When and where did India and Asia collide?, *J. Geophys. Res.*, 112, B05423, doi:10.1029/2006JB004706.
- Allègre, C. J., et al. (1984), Structure and evolution of the Himalaya-Tibet orogenic belt, *Nature*, 307(5946), 17–22, doi:10.1038/307017a0.
- Argand, E. (1924), La tectonique de l'Asie, *Int. Geol. Congr.*, 13, 170–372.
- Barazangi, M., and J. Ni (1982), Velocities and propagation characteristics of Pn and Sn beneath the Himalayan arc and Tibetan Plateau: Possible evidence for underthrusting of Indian continental lithosphere beneath Tibet, *Geology*, 10(4), 179–185, doi:10.1130/0091-7613(1982)10<179:VAPCOP>2.0.CO;2.
- Barron, J., and K. Priestley (2009), Observations of frequency-dependent Sn propagation in northern Tibet, *Geophys. J. Int.*, 179(1), 475–488, doi:10.1111/j.1365-246X.2009.04318.x.
- Bartzsch, S., S. Lebedev, and T. Meier (2011), Resolving the lithosphere-asthenosphere boundary with seismic Rayleigh waves, *Geophys. J. Int.*, 186(3), 1152–1164, doi:10.1111/j.1365-246X.2011.05096.x.
- Bijwaard, H., W. Spakman, and E. R. Engdahl (1998), Closing the gap between regional and global travel time tomography, *J. Geophys. Res.*, 103(B12), 30,055–30,078, doi:10.1029/98JB02467.
- Brandon, C., and B. Romanowicz (1986), A no-lid zone in the Central Chang-Thang Platform of Tibet: Evidence from pure path phase velocity measurements of long period Rayleigh waves, *J. Geophys. Res.*, 91(B6), 6547–6564, doi:10.1029/JB091iB06p06547.
- Ceylan, S., J. Ni, J. Y. Chen, Q. Zhang, F. Tilmann, and E. Sandvol (2012), Fragmented Indian plate and vertically coherent deformation beneath eastern Tibet, *J. Geophys. Res.*, 117, B11303, doi:10.1029/2012JB009210.
- Chemenda, A. I., J.-P. Burg, and M. Mattauer (2000), Evolutionary model of the Himalaya-Tibet system: Geopembased on new modelling, geological and geophysical data, *Earth Planet. Sci. Lett.*, 174(3–4), 397–409, doi:10.1016/S0012-821X(99)00277-0.
- Clark, M. K. (2012), Continental collision slowing due to viscous mantle lithosphere rather than topography, *Nature*, 483(7387), 74–77, doi:10.1038/nature10848.
- Cobden, L., S. Goes, F. Cammarano, and J. A. D. Connolly (2008), Thermochemical interpretation of one-dimensional seismic reference models for the upper mantle: Evidence for bias due to heterogeneity, *Geophys. J. Int.*, 175(2), 627–648, doi:10.1111/j.1365-246X.2008.03903.x.
- Connolly, J. A. D. (2005), Computation of phase equilibria by linear programming: A tool for geodynamic modeling and its application to subduction zone decarbonation, *Earth Planet. Sci. Lett.*, 236(1–2), 524–541, doi:10.1016/j.epsl.2005.04.033.
- Curtis, A., and J. H. Woodhouse (1997), Crust and upper mantle shear velocity structure beneath the Tibetan Plateau and surrounding regions from interevent surface wave phase velocity inversion, *J. Geophys. Res.*, 102(B6), 11,789–11,813, doi:10.1029/96JB03182.
- Deal, M. M., G. Nolet, and R. D. van der Hilst (1999), Slab temperature and thickness from seismic tomography: 1. Method and application to Tonga, *J. Geophys. Res.*, 104(B12), 28,789–28,802, doi:10.1029/1999JB900255.
- Dewey, J. F., R. M. Shackleton, C. Chengfa, and S. Yiyin (1988), The tectonic evolution of the Tibetan Plateau, *Philos. Trans. R. Soc. London, Ser. A*, 327(1594), 379–413, doi:10.1098/rsta.1988.0135.
- Endrun, B., T. Meier, S. Lebedev, M. Bohnhoff, G. Stavrakakis, and H.-p. Harjes (2008), S velocity structure and radial anisotropy in the Aegean region from surface wave dispersion, *Geophys. J. Int.*, 174(2), 593–616, doi:10.1111/j.1365-246X.2008.03802.x.



- England, P., and G. Houseman (1986), Finite strain calculations of continental deformation: 2. Comparison with the India-Asia collision zone, *J. Geophys. Res.*, *91*(B3), 3664–3676, doi:10.1029/JB091iB03p03664.
- England, P., and M. Searle (1986), The Cretaceous-tertiary deformation of the Lhasa Block and its implications for crustal thickening in Tibet, *Tectonics*, *5*(1), 1–14, doi:10.1029/TC005i001p00001.
- Friederich, W. (2003), The S-velocity structure of the East Asian mantle from inversion of shear and surface waveforms, *Geophys. J. Int.*, *153*(1), 88–102, doi:10.1046/j.1365-246X.2003.01869.x.
- Fullea, J., J. C. Afonso, J. A. D. Connolly, M. Fernández, D. García-Castellanos, and H. Zeyen (2009), LitMod3D: An interactive 3-D software to model the thermal, compositional, density, seismological, and rheological structure of the lithosphere and sublithospheric upper mantle, *Geochem. Geophys. Geosyst.*, *10*, Q08019, doi:10.1029/2009GC002391.
- Fullea, J., S. Lebedev, M. R. Agius, A. G. Jones, and J. C. Afonso (2012), Lithospheric structure in the Baikal-central Mongolia region from integrated geophysical-petrological inversion of surface-wave data and topographic elevation, *Geochem. Geophys. Geosyst.*, *13*, Q0AK09, doi:10.1029/2012GC004138.
- Griot, D.-A., J.-P. Montagner, and P. Tapponnier (1998), Phase velocity structure from Rayleigh and Love waves in Tibet and its neighboring regions, *J. Geophys. Res.*, *103*(B9), 21,215–21,232, doi:10.1029/98JB00953.
- Guillot, S., E. Garzanti, D. Baratoux, D. Marquer, G. Maheo, and J. de Sigoyer (2003), Reconstructing the total shortening history of the NW Himalaya, *Geochem. Geophys. Geosyst.*, *4*(7), 1064, doi:10.1029/2002GC000484.
- Gupta, S., S. S. Rai, K. S. Prakasam, D. Srinagesh, B. K. Bansal, R. K. Chadha, K. Priestley, and V. K. Gaur (2003), The nature of the crust in southern India: Implications for Precambrian crustal evolution, *Geophys. Res. Lett.*, *30*(8), 1419, doi:10.1029/2002GL016770.
- Hafkenschied, E., M. J. R. Wortel, and W. Spakman (2006), Subduction history of the Tethyan region derived from seismic tomography and tectonic reconstructions, *J. Geophys. Res.*, *111*, B08401, doi:10.1029/2005JB003791.
- Hanna, A. C., and D. S. Weeraratne (2013), Surface wave velocity structure of the western Himalayan syntaxis, *Geophys. J. Int.*, *194*(3), 1866–1877, doi:10.1093/gji/ggt203.
- Hatzfeld, D., and P. Molnar (2010), Comparisons of the kinematics and deep structures of the Zagros and Himalaya and of the Iranian and Tibetan Plateaus and geodynamic implications, *Rev. Geophys.*, *48*, RG2005, doi:10.1029/2009RG000304.
- Hearn, T. M., S. Wang, J. F. Ni, Z. Xu, Y. Yu, and X. Zhang (2004), Uppermost mantle velocities beneath China and surrounding regions, *J. Geophys. Res.*, *109*, B11301, doi:10.1029/2003JB002874.
- Houseman, G. A., D. P. McKenzie, and P. Molnar (1981), Convective instability of a thickened boundary layer and its relevance for the thermal evolution of continental convergent belts, *J. Geophys. Res.*, *86*(B7), 6115–6132, doi:10.1029/JB086iB07p06115.
- Huang, J., and D. Zhao (2006), High-resolution mantle tomography of China and surrounding regions, *J. Geophys. Res.*, *111*, B09305, doi:10.1029/2005JB004066.
- Huang, W.-C., J. F. Ni, F. Tilmann, D. Nelson, J. Guo, W. Zhao, J. Mechie, R. Kind, J. Saul, R. Rapine, and T. M. Hearn (2000), Seismic polarization anisotropy beneath the central Tibetan Plateau, *J. Geophys. Res.*, *105*(B12), 27,979–27,989, doi:10.1029/2000JB900339.
- Jiménez-Munt, I., M. Fernández, J. Vergés, and J. P. Platt (2008), Lithosphere structure underneath the Tibetan Plateau inferred from elevation, gravity and geoid anomalies, *Earth Planet. Sci. Lett.*, *267*(1–2), 276–289, doi:10.1016/j.epsl.2007.11.045.
- Kennett, B. L. N., E. R. Engdahl, and R. Buland (1995), Constraints on seismic velocities in the Earth from traveltimes, *Geophys. J. Int.*, *122*(1), 108–124, doi:10.1111/j.1365-246X.1995.tb03540.x.
- Kind, R., and X. Yuan (2010), Seismic images of the biggest crash on Earth., *Science*, *329*(5998), 1479–1480, doi:10.1126/science.1191620.
- Kind, R., et al. (2002), Seismic images of crust and upper mantle beneath Tibet: Evidence for Eurasian plate subduction, *Science*, *298*(5596), 1219–1221, doi:10.1126/science.1078115.
- Klemperer, S. L., B. M. Kennedy, S. R. Sastry, Y. Makovsky, T. Harinarayana, and M. L. Leech (2013), Mantle fluids in the Karakoram fault: Helium isotope evidence, *Earth Planet. Sci. Lett.*, *366*, 59–70, doi:10.1016/j.epsl.2013.01.013.
- Kosarev, G., R. Kind, S. V. Sobolev, X. Yuan, W. Hanka, and S. Oreshin (1999), Seismic evidence for a detached Indian lithospheric mantle beneath Tibet, *Science*, *283*(5406), 1306–1309, doi:10.1126/science.283.5406.1306.
- Kumar, P., X. Yuan, R. Kind, and J. Ni (2006), Imaging the colliding Indian and Asian lithospheric plates beneath Tibet, *J. Geophys. Res.*, *111*, B06308, doi:10.1029/2005JB003930.
- Kustowski, B., G. Ekström, and A. M. Dziewoski (2008), The shear-wave velocity structure in the upper mantle beneath Eurasia, *Geophys. J. Int.*, *174*(3), 978–992, doi:10.1111/j.1365-246X.2008.03865.x.
- Lebedev, S., and R. D. van der Hilst (2008), Global upper-mantle tomography with the automated multimode inversion of surface and S-wave forms, *Geophys. J. Int.*, *173*(2), 505–518, doi:10.1111/j.1365-246X.2008.03721.x.
- Lebedev, S., G. Nolet, T. Meier, and R. D. van der Hilst (2005), Automated multimode inversion of surface and S waveforms, *Geophys. J. Int.*, *162*(3), 951–964, doi:10.1111/j.1365-246X.2005.02708.x.
- Lebedev, S., T. Meier, and R. D. van der Hilst (2006), Asthenospheric flow and origin of volcanism in the Baikal Rift area, *Earth Planet. Sci. Lett.*, *249*(3–4), 415–424, doi:10.1016/j.epsl.2006.07.007.
- Lebedev, S., J. Boonen, and J. Trampert (2009), Seismic structure of Precambrian lithosphere: New constraints from broad-band surface-wave dispersion, *Lithos*, *109*(1–2), 96–111, doi:10.1016/j.lithos.2008.06.010.
- Leon Soto, G., E. Sandvol, J. F. Ni, L. M. Flesch, T. M. Hearn, F. Tilmann, Y. J. Chen, and L. Brown (2012), Significant and vertically coherent seismic anisotropy beneath eastern Tibet, *J. Geophys. Res.*, *117*, B05308, doi:10.1029/2011JB008919.
- Li, C., R. D. van der Hilst, A. S. Meltzer, and E. R. Engdahl (2008), Subduction of the Indian lithosphere beneath the Tibetan Plateau and Burma, *Earth Planet. Sci. Lett.*, *274*(1–2), 157–168, doi:10.1016/j.epsl.2008.07.016.
- Li, S., W. D. Mooney, and J. Fan (2006), Crustal structure of mainland China from deep seismic sounding data, *Tectonophysics*, *420*, 239–252, doi:10.1016/j.tecto.2006.01.026.
- Liang, C., and X. Song (2006), A low velocity belt beneath northern and eastern Tibetan Plateau from Pn tomography, *Geophys. Res. Lett.*, *33*, L22306, doi:10.1029/2006GL027926.



- Liang, C., X. Song, and J. Huang (2004), Tomographic inversion of Pn travel times in China, *J. Geophys. Res.*, *109*, B11304, doi:10.1029/2003JB002789.
- Liang, X., Y. Shen, Y. J. Chen, and Y. Ren (2011), Crustal and mantle velocity models of southern Tibet from finite frequency tomography, *J. Geophys. Res.*, *116*, B02408, doi:10.1029/2009JB007159.
- Liang, X., E. Sandvol, Y. J. Chen, T. Hearn, J. Ni, S. Klemperer, Y. Shen, and F. Tilmann (2012), A complex Tibetan upper mantle: A fragmented Indian slab and no south-verging subduction of Eurasian lithosphere, *Earth Planet. Sci. Lett.*, *333–334*, 101–111, doi:10.1016/j.epsl.2012.03.036.
- Liu, M., W. D. Mooney, S. Li, N. Okaya, and S. Detweiler (2006), Crustal structure of the northeastern margin of the Tibetan Plateau from the Songpan-Ganzi terrane to the Ordos basin, *Tectonophysics*, *420(1–2)*, 253–266, doi:10.1016/j.tecto.2006.01.025.
- McKenzie, D., and K. Priestley (2008), The influence of lithospheric thickness variations on continental evolution, *Lithos*, *102(1–2)*, 1–11, doi:10.1016/j.lithos.2007.05.005.
- McNamara, D. E., T. J. Owens, and W. R. Walter (1995), Observations of regional phase propagation across the Tibetan Plateau, *J. Geophys. Res.*, *100(B11)*, 22,215–22,229, doi:10.1029/95JB01863.
- McNamara, D. E., W. R. Walter, T. J. Owens, and C. J. Ammon (1997), Upper mantle velocity structure beneath the Tibetan Plateau from Pn travel time tomography, *J. Geophys. Res.*, *102(B1)*, 493–505, doi:10.1029/96JB02112.
- Meier, T., K. Dietrich, B. Stöckhert, and H.-P. Harjes (2004), One-dimensional models of shear wave velocity for the eastern Mediterranean obtained from the inversion of Rayleigh wave phase velocities and tectonic implications, *Geophys. J. Int.*, *156(1)*, 45–58, doi:10.1111/j.1365-246X.2004.02121.x.
- Meissner, R., F. Tilmann, and S. Haines (2004), About the lithospheric structure of central Tibet, based on seismic data from the INDEPTH III profile, *Tectonophysics*, *380(1–2)*, 1–25, doi:10.1016/j.tecto.2003.11.007.
- Molnar, P., and P. Tapponnier (1975), Cenozoic tectonics of Asia: Effects of a continental collision, *Science*, *189(4201)*, 419–426, doi:10.1126/science.189.4201.419.
- Molnar, P., P. England, and J. Martinod (1993), Mantle dynamics, uplift of the Tibetan Plateau, and the Indian Monsoon, *Rev. Geophys.*, *31(4)*, 357–396, doi:10.1029/93RG02030.
- Nábelek, J., G. Hetényi, J. Vergne, S. Sapkota, B. Kafle, M. Jiang, H. Su, J. Chen, B.-S. Huang, and the Hi-CLIMB Team (2009), Underplating in the Himalaya-Tibet collision zone revealed by the Hi-CLIMB experiment., *Science*, *325(5946)*, 1371–4, doi:10.1126/science.1167719.
- Nelson, K. D., et al. (1996), Partially molten middle crust beneath southern Tibet: Synthesis of project INDEPTH results, *Science*, *274(5293)*, 1684–1688, doi:10.1126/science.274.5293.1684.
- Ni, J., and M. Barazangi (1984), Seismotectonics of the Himalayan collision zone: Geometry of the underthrusting Indian Plate beneath the Himalaya, *J. Geophys. Res.*, *89(B2)*, 1147–1163, doi:10.1029/JB089iB02p01147.
- Oreshin, S., S. Kiselev, L. Vinnik, K. Surya Prakasam, S. S. Rai, L. Makeyeva, and Y. Savvin (2008), Crust and mantle beneath western Himalaya, Ladakh and western Tibet from integrated seismic data, *Earth Planet. Sci. Lett.*, *271(1–4)*, 75–87, doi:10.1016/j.epsl.2008.03.048.
- Owens, T. J., and G. Zandt (1997), Implications of crustal property variations for models of Tibetan Plateau evolution, *Nature*, *387(6628)*, 37–43, doi:10.1038/387037a0.
- Owens, T. J., G. E. Randall, F. T. Wu, and R. Zeng (1993), PASSCAL instrument performance during the Tibetan Plateau passive seismic experiment, *Bull. Seismol. Soc. Am.*, *83*, 1959–1970.
- Panning, M. P., A. Cao, A. Kim, and B. A. Romanowicz (2012), Non-linear 3-D Born shear waveform tomography in southeast Asia, *Geophys. J. Int.*, *190(1)*, 463–475, doi:10.1111/j.1365-246X.2012.05489.x.
- Pedersen, H. A. (2006), Impacts of non-plane waves on two-station measurements of phase velocities, *Geophys. J. Int.*, *165(1)*, 279–287, doi:10.1111/j.1365-246X.2006.02893.x.
- Pei, S., J. Zhao, Y. Sun, Z. Xu, S. Wang, H. Liu, C. A. Rowe, M. N. Toksöz, and X. Gao (2007), Upper mantle seismic velocities and anisotropy in China determined through Pn and Sn tomography, *J. Geophys. Res.*, *112*, B05312, doi:10.1029/2006JB004409.
- Phillips, W. S., C. A. Rowe, and L. K. Steck (2005), The use of interstation P wave arrival time differences to account for regional path variability, *Geophys. Res. Lett.*, *32*, L11301, doi:10.1029/2005GL022558.
- Powell, C. (1986), Continental underplating model for the rise of the Tibetan Plateau, *Earth Planet. Sci. Lett.*, *81(1)*, 79–94, doi:10.1016/0012-821X(86)90102-0.
- Priestley, K., E. Debayle, D. McKenzie, and S. Pilidou (2006), Upper mantle structure of eastern Asia from multimode surface waveform tomography, *J. Geophys. Res.*, *111*, B10304, doi:10.1029/2005JB004082.
- Priestley, K., J. Jackson, and D. McKenzie (2008), Lithospheric structure and deep earthquakes beneath India, the Himalaya and southern Tibet, *Geophys. J. Int.*, *172(1)*, 345–362, doi:10.1111/j.1365-246X.2007.03636.x.
- Rai, S., K. Priestley, K. Suryaprakasam, D. Srinagesh, V. K. Gaur, and Z. Du (2003), Crustal shear velocity structure of the south Indian shield, *J. Geophys. Res.*, *108(B2)*, 2088, doi:10.1029/2002JB001776.
- Rapine, R., F. Tilmann, M. West, J. Ni, and A. Rodgers (2003), Crustal structure of northern and southern Tibet from surface wave dispersion analysis, *J. Geophys. Res.*, *108(B2)*, 2120, doi:10.1029/2001JB000445.
- Replumaz, A., A. M. Negrodo, A. Villaseñor, and S. Guillot (2010a), Indian continental subduction and slab break-off during Tertiary collision, *Terra Nova*, *22(4)*, 290–296, doi:10.1111/j.1365-3121.2010.00945.x.
- Replumaz, A., A. M. Negrodo, S. Guillot, and A. Villaseñor (2010b), Multiple episodes of continental subduction during India/Asia convergence: Insight from seismic tomography and tectonic reconstruction, *Tectonophysics*, *483(1–2)*, 125–134, doi:10.1016/j.tecto.2009.10.007.
- Ritzwoller, M. H., M. P. Barmin, A. Villaseñor, A. L. Levshin, and E. Engdahl (2002), Pn and Sn tomography across Eurasia to improve regional seismic event locations, *Tectonophysics*, *358(1–4)*, 39–55, doi:10.1016/S0040-1951(02)00416-X.
- Romanowicz, B. A. (1982), Constraints on the structure of the Tibet Plateau from pure path phase velocities of Love and Rayleigh waves, *J. Geophys. Res.*, *87(B8)*, 6865–6883, doi:10.1029/JB087iB08p06865.
- Royden, L. H., B. C. Burchfiel, and R. D. v. d. Hilst (2008), The geological evolution of the Tibetan Plateau, *Science*, *321(5892)*, 1054–1058, doi:10.1126/science.1155371.
- Schaeffer, A., and S. Lebedev (2013), Global shear speed structure of the upper mantle and transition zone, *Geophys. J. Int.*, *194(1)*, 417–449, doi:10.1093/gji/ggt095.
- Schutt, D. L., and C. E. Leshner (2006), Effects of melt depletion on the density and seismic velocity of garnet and spinel



- lherzolite, *J. Geophys. Res.*, *111*, B05401, doi:10.1029/2003JB002950.
- Shapiro, N. M., and M. H. Ritzwoller (2002), Monte-Carlo inversion for a global shear-velocity model of the crust and upper mantle, *Geophys. J. Int.*, *151*(1), 88–105, doi:10.1046/j.1365-246X.2002.01742.x.
- Shapiro, N. M., M. H. Ritzwoller, P. Molnar, and V. Levin (2004), Thinning and flow of Tibetan crust constrained by seismic anisotropy, *Science*, *305*(5681), 233–236, doi:10.1126/science.1098276.
- Sol, S., et al. (2007), Geodynamics of the southeastern Tibetan Plateau from seismic anisotropy and geodesy, *Geology*, *35*(6), 563–566, doi:10.1130/G23408A.1.
- Stixrude, L., and C. Lithgow-Bertelloni (2007), Influence of phase transformations on lateral heterogeneity and dynamics in Earth's mantle, *Earth Planet. Sci. Lett.*, *263*(1–2), 45–55, doi:10.1016/j.epsl.2007.08.027.
- Sun, Y., and M. N. Toksöz (2006), Crustal structure of China and surrounding regions from P wave traveltime tomography, *J. Geophys. Res.*, *111*, B03310, doi:10.1029/2005JB003962.
- Sun, Y., M. N. Toksoz, S. Pei, and F. D. Morgan (2008a), The layered shear-wave velocity structure of the crust and uppermost mantle in China, *Bull. Seismol. Soc. Am.*, *98*(2), 746–755, doi:10.1785/0120050222.
- Sun, Y., M. N. Toksöz, S. Pei, D. Zhao, F. D. Morgan, and A. Rosca (2008b), S wave tomography of the crust and uppermost mantle in China, *J. Geophys. Res.*, *113*, B11307, doi:10.1029/2008JB005836.
- Tapponnier, P., X. Zhiqin, F. Roger, B. Meyer, N. Arnaud, G. Wittlinger, and Y. Jingsui (2001), Oblique stepwise rise and growth of the Tibet Plateau., *Science*, *294*(5547), 1671–1677, doi:10.1126/science.105978.
- Tilmann, F., J. Ni, and INDEPTH III Seismic Team (2003), Seismic imaging of the downwelling Indian lithosphere beneath central Tibet., *Science*, *300*(5624), 1424–1427, doi:10.1126/science.1082777.
- Tseng, T.-I., W.-p. Chen, and R. L. Nowack (2009), Northward thinning of Tibetan crust revealed by virtual seismic profiles, *Geophys. Res. Lett.*, *36*, L24304, doi:10.1029/2009GL040457.
- Van der Voo, R., W. Spakman, and H. Bijwaard (1999), Tethyan subducted slabs under India, *Earth Planet. Sci. Lett.*, *171*(1), 7–20, doi:10.1016/S0012-821X(99)00131-4.
- van Hinsbergen, D. J. J., B. Steinberger, P. V. Doubrovine, and R. Gassmüller (2011), Acceleration and deceleration of India-Asia convergence since the Cretaceous: Roles of mantle plumes and continental collision, *J. Geophys. Res.*, *116*, B06101, doi:10.1029/2010JB008051.
- van Hinsbergen, D. J. J., P. C. Lippert, G. Dupont-Nivet, N. McQuarrie, P. V. Doubrovine, W. Spakman, and T. H. Torsvik (2012), Greater India Basin hypothesis and a two-stage Cenozoic collision between India and Asia., *Proc. Natl. Acad. Sci. U. S. A.*, *109*(20), 7659–64, doi:10.1073/pnas.1117262109.
- Wessel, P., and W. H. F. Smith (1998), New, improved version of generic mapping tools released, *Eos Trans. AGU*, *79*(47), 579–579, doi:10.1029/98EO00426.
- Willett, S. D., and C. Beaumont (1994), Subduction of Asian lithospheric mantle beneath Tibet inferred from models of continental collision, *Nature*, *369*(6482), 642–645, doi:10.1038/369642a0.
- Wittlinger, G., V. Farra, and J. Vergne (2004), Lithospheric and upper mantle stratifications beneath Tibet: New insights from Sp conversions, *Geophys. Res. Lett.*, *31*, L19615, doi:10.1029/2004GL020955.
- Yin, A., and T. M. Harrison (2000), Geologic evolution of the Himalayan-Tibetan Orogen, *Annu. Rev. Earth Planet. Sci.*, *28*(1), 211–280, doi:10.1146/annurev.earth.28.1.211.
- Yue, H., et al. (2012), Lithospheric and upper mantle structure of the northeastern Tibetan Plateau, *J. Geophys. Res.*, *117*, B05307, doi:10.1029/2011JB008545.
- Zahirovic, S., R. D. Müller, M. Seton, N. Flament, M. Gurnis, and J. Whittaker (2012), Insights on the kinematics of the India-Eurasia collision from global geodynamic models, *Geochem. Geophys. Geosyst.*, *13*, Q04W11, doi:10.1029/2011GC003883.
- Zhang, H., D. Zhao, J. Zhao, and Q. Xu (2012), Convergence of the Indian and Eurasian plates under eastern Tibet revealed by seismic tomography, *Geochem. Geophys. Geosyst.*, *13*, Q06W14, doi:10.1029/2012GC004031.
- Zhang, Q., E. Sandvol, J. Ni, Y. Yang, and Y. J. Chen (2011), Rayleigh wave tomography of the northeastern margin of the Tibetan Plateau, *Earth Planet. Sci. Lett.*, *304*(1–2), 103–112, doi:10.1016/j.epsl.2011.01.021.
- Zhang, Z., and S. L. Klemperer (2005), West-east variation in crustal thickness in northern Lhasa block, central Tibet, from deep seismic sounding data, *J. Geophys. Res.*, *110*, B09403, doi:10.1029/2004JB003139.
- Zhao, J., et al. (2010), The boundary between the Indian and Asian tectonic plates below Tibet., *Proc. Natl. Acad. Sci. U. S. A.*, *107*(25), 11,229–11,233, doi:10.1073/pnas.1001921107.
- Zhao, W., et al. (2001), Crustal structure of central Tibet as derived from project INDEPTH wide-angle seismic data, *Geophys. J. Int.*, *145*(2), 486–498, doi:10.1046/j.0956-540x.2001.01402.x.
- Zhao, W., et al. (2011), Tibetan plate overriding the Asian plate in central and northern Tibet, *Nat. Geosci.*, *4*(12), 870–873, doi:10.1038/ngeo1309.
- Zhou, H.-W., and M. A. Murphy (2005), Tomographic evidence for wholesale underthrusting of India beneath the entire Tibetan Plateau, *J. Asian Earth Sci.*, *25*(3), 445–457, doi:10.1016/j.jseas.2004.04.007.